

Jefferson Lab PAC 39 Proposal

**The Longitudinal Photon, Transverse Nucleon, Single-Spin  
Asymmetry in Exclusive Pion Electroproduction**

May 4, 2012

K. Hafidi

*Argonne National Laboratory, Argonne, IL 60439 USA*

K. Aniol

*California State University Los Angeles, Los Angeles, CA 90032 USA*

P. Markowitz

*Florida International University, Miami, FL 33199 USA*

A.K. Opper

*George Washington University, Washington, DC 20052 USA*

A. Camsonne, H.C. Fenker, D.J. Gaskell (Co-spokesperson), M.K. Jones,

A. Kalyan, D.J. Mack, B. Sawatzky, P. Solvignon, S.A. Wood

*Jefferson Lab, Newport News, VA 23606 USA*

M. Mihovilovič, S. Širca

*Jožef Stefan Institute and University of Ljubljana, Ljubljana, Slovenia*

Xin Qian

*Kellogg Radiation Lab, California Institute of Technology, Pasadena, CA, 91106*

J. Dunne, D. Dutta (Co-spokesperson), A. Narayan, L. Ndukum,

M. Shabestari, A. Subedi, Li Ye

*Mississippi State University, Mississippi State, MS 39762 USA*

D.L. Hornidge

*Mount Allison University, Sackville, NB E4L-1E4 Canada*

F.W. Hersman (Co-spokesperson)

*University of New Hampshire, Durham, NH 03824 USA*

A. Ahmidouch, S. Danagoulian

*North Carolina A&T State University, Greensboro, NC 27411 USA*

E. Korkmaz

*University of Northern British Columbia, Prince George, BC V2N-4Z9 Canada*

P.M. King, J. Roche

*Ohio University, Athens, OH 45701 USA*

G.M. Huber (Co-spokesperson), W. Li, Z. Papandreou, A. Semenov

*University of Regina, Regina, SK S4S-0A2 Canada*

A.J. Sarty

*Saint Mary's University, Halifax, NS B3H-3C3 Canada*

H. Baghdasaryan, M. Dalton

*University of Virginia, Charlottesville, VA 22904 USA*

F.R. Wesselmann

*Xavier University of Louisiana, New Orleans, LA 70125 USA*

We propose to measure the longitudinal photon, transverse nucleon, single-spin asymmetry in the exclusive pion production  $\vec{n}(e, e'\pi^-)p$  reaction, using a transversely polarized  $^3\text{He}$  target. This polarization observable has been noted as being especially sensitive to the spin-flip generalized parton distribution (GPD)  $\tilde{E}$ , and factorization studies have indicated that precocious scaling is likely to set in at moderate  $Q^2 \sim 2 - 4 \text{ GeV}^2$ , as opposed to the absolute cross section, where scaling is not expected until  $Q^2 > 10 \text{ GeV}^2$ . Furthermore, this observable has been noted as being important for the reliable extraction of the charged pion form factor from pion electroproduction. We intend to pursue this study using the SHMS-HMS spectrometer combination in Hall C. In order to reduce the total beamtime requirement, we propose to use a next generation, externally polarized, continuous flow, high luminosity  $^3\text{He}$  target based on a large volume polarizer and compressor developed at the University of New Hampshire. A crucial aspect of our experiment is the Rosenbluth L-T separation. Unlike other ongoing or proposed experiments, where the dominance of the longitudinal contribution to the spin asymmetry at intermediate  $Q^2$  is simply assumed, we intend to demonstrate whether this is in fact the case. This is important, because factorization has only been proven for the case of longitudinal photons. Data from this experiment will thus indicate whether the precocious scaling expectations of the GPD formalism will be ultimately realized, as well as helping to constrain longitudinal backgrounds possibly complicating the extraction of the pion form factor from electroproduction experiment data.

## I. SCIENTIFIC JUSTIFICATION

### A. Generalized Parton Distributions and Contribution from the Pion Pole

In recent years, much progress has been made in the theory of generalized parton distributions (GPDs). Unifying the concepts of parton distributions and of hadronic form factors, they contain a wealth of information about how quarks and gluons make up hadrons. The key difference between the usual parton distributions and their generalized counterparts can be seen by representing them in terms of the quark and gluon wavefunctions of the hadron. While the usual parton distributions are obtained from the squared hadron wavefunction representing the probability to find a parton with specified polarization and longitudinal momentum fraction  $x$  in the fast moving hadron (Fig. 1a), GPDs represent the interference of different wavefunctions, one where the parton has momentum fraction  $x + \xi$  and one where this fraction is  $x - \xi$  (Fig. 1b). GPDs thus correlate different parton configurations in the hadron at the quantum mechanical level. A special kinematic regime is probed in deep exclusive meson production, where the initial hadron emits a quark-antiquark or gluon pair (Fig. 1c). This has no counterpart in the usual parton distributions and carries information about  $q\bar{q}$  and  $gg$ -components in the hadron wavefunction.

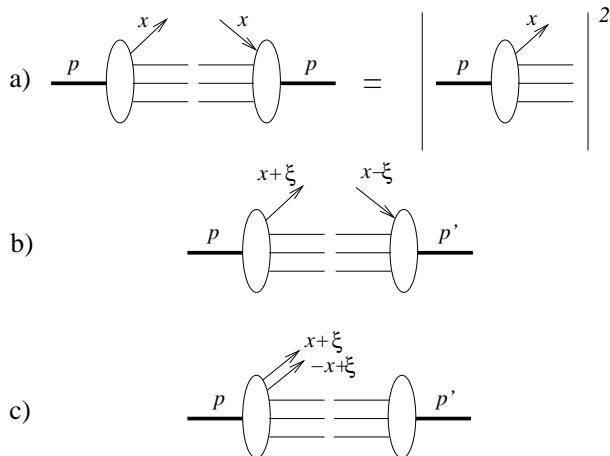


FIG. 1: (a) Usual parton distribution, representing the probability to find a parton with momentum fraction  $x$  in the nucleon. (b) GPD in the region where it represents the emission of a parton with momentum fraction  $x + \xi$  and its reabsorption with momentum fraction  $x - \xi$ . (c) GPD in the region where it represents the emission of a quark-antiquark pair, and has no counterpart in the usual parton distributions. This figure has been adapted from Ref. [1].

Apart from the momentum fraction variables  $x$  and  $\xi$ , GPDs depend on the four momentum transfer  $t$ . This is an independent variable, because the momenta  $p$  and  $p'$  may differ in either their longitudinal or transverse components. GPDs thus interrelate the longitudinal and transverse momentum structure of partons within a fast moving hadron.

In order to access the physics contained within GPDs, one is restricted to the hard scattering regime. An important feature of hard scattering reactions is the possibility to separate clearly the perturbative and nonperturbative stages of the interaction. Qualitatively speaking, the presence of a hard probe allows one to create small size quark-antiquark and gluon configurations, whose interactions are described by perturbative QCD (pQCD). The non-perturbative stage of the reaction describes how the hadron reacts to this configuration, or how this probe is transformed into hadrons. This separation is the so-called factorization property of hard reactions. Hard exclusive meson electroproduction was first shown to be factorizable in Ref. [2]. This factorization applies when the virtual photon is longitudinally polarized, which is more probable to produce a small size configuration compared to a transversely polarized photon.

GPDs are universal quantities and reflect the structure of the nucleon independently of the reaction which probes the nucleon. At leading twist-2 level, the nucleon structure information can be parameterized in terms of four quark chirality conserving GPDs, denoted  $H$ ,  $E$ ,  $\tilde{H}$  and  $\tilde{E}$ .  $H$  and  $E$  are summed over quark helicity, while  $\tilde{H}$  and  $\tilde{E}$  involve the difference between left and right handed quarks.  $H$  and  $\tilde{H}$  conserve the helicity of the proton, while  $E$  and  $\tilde{E}$  allow for the possibility that the proton helicity is flipped. Because quark helicity is conserved in the hard scattering regime, the produced meson acts as a helicity filter. In particular, leading order QCD predicts that vector meson production is sensitive only to the unpolarized GPDs,  $H$  and  $E$ , whereas pseudoscalar meson production is sensitive only to the polarized GPDs,  $\tilde{H}$  and  $\tilde{E}$ . In contrast, deeply virtual Compton scattering (DVCS) depends at the same time on both the polarized ( $\tilde{H}$  and  $\tilde{E}$ ) and the unpolarized ( $H$  and  $E$ ) GPDs. This makes exclusive hard meson electroproduction reactions complementary to the DVCS process, as it provides an additional tool to disentangle the different GPDs [3].

Besides coinciding with the parton distributions at vanishing momentum transfer  $\xi$ , the GPDs have interesting links with other nucleon structure quantities. Their first moments are related to the elastic form factors of the nucleon through model-independent sum rules

[4]:

$$\sum_q e_q \int_{-1}^{+1} dx H^q(x, \xi, t) = F_1(t), \quad (1)$$

$$\sum_q e_q \int_{-1}^{+1} dx E^q(x, \xi, t) = F_2(t), \quad (2)$$

$$\sum_q e_q \int_{-1}^{+1} dx \tilde{H}^q(x, \xi, t) = G_A(t), \quad (3)$$

$$\sum_q e_q \int_{-1}^{+1} dx \tilde{E}^q(x, \xi, t) = G_P(t), \quad (4)$$

where  $e_q$  is the charge of the relevant quark,  $F_1(t)$ ,  $F_2(t)$  are the Dirac and Pauli elastic nucleon form factors, and  $G_A(t)$ ,  $G_P(t)$  are the isovector axial and pseudoscalar nucleon form factors. The  $t$ -dependence of  $G_A(t)$  is poorly known, and although  $G_P(t)$  is an important quantity, it remains highly uncertain because it is negligible at the momentum transfer of  $\beta$ -decay[5]. Because of partial conservation of the axial current (PCAC),  $G_P(t)$  alone receives contributions from  $J^{PG} = 0^{--}$  states[6], which are the quantum numbers of the pion, and so  $\tilde{E}$  contains an important pion pole contribution (Fig. 2a).

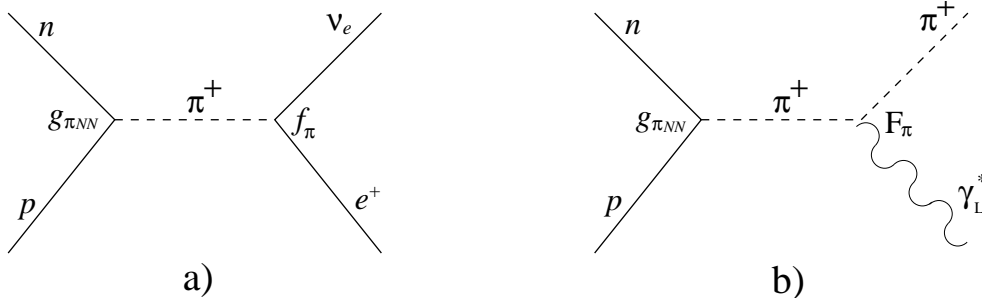


FIG. 2: (a) Pion pole contribution to  $G_P(t)$ , and hence to  $\tilde{E}$ . (b) Pion pole contribution to meson electroproduction at low  $-t$ .

Accordingly, Refs. [7, 8] have adopted the pion pole-dominated ansatz

$$\tilde{E}^{ud}(x, \xi, t) = F_{\pi}(t) \frac{\theta(\xi > |x|)}{2\xi} \phi_{\pi}\left(\frac{x + \xi}{2\xi}\right), \quad (5)$$

where  $F_{\pi}(t)$  is the pion electromagnetic form factor, and  $\phi_{\pi}$  is the pion distribution amplitude.

$\tilde{E}$  cannot be related to already known parton distributions, and so experimental information about  $\tilde{E}$  via hard pion electroproduction can provide new information on nucleon structure which is unlikely to be available from any other source.

## B. Single spin asymmetry in exclusive pion electroproduction

Frankfurt et al. [9] have considered a specific polarization observable which is the most sensitive observable to probe the spin-flip  $\tilde{E}$ . This variable is the single-spin asymmetry for exclusive charged pion production,  $\vec{p}(e, e'\pi^+)n$  or  $\vec{n}(e, e'\pi^-)p$ , from a transversely polarized nucleon target, and is defined [8] as

$$A_L^\perp = \left( \int_0^\pi d\beta \frac{d\sigma_L^\pi}{d\beta} - \int_\pi^{2\pi} d\beta \frac{d\sigma_L^\pi}{d\beta} \right) \left( \int_0^{2\pi} d\beta \frac{d\sigma_L^\pi}{d\beta} \right)^{-1}, \quad (6)$$

where  $d\sigma_L^\pi$  is the exclusive charged pion electroproduction cross section using longitudinally polarized photons and  $\beta$  is the angle between the nucleon polarization vector and the reaction plane. Frankfurt et al. [9] have shown that this asymmetry must vanish if  $\tilde{E}$  is zero. If  $\tilde{E}$  is not zero, the asymmetry will display a  $\sin\beta$  dependence. Their predicted asymmetry using the  $\tilde{E}$  ansatz from Ref. [10] is shown in Fig. 3. This calculation is  $Q^2$ -independent, depending only on how well the soft contributions cancel in the asymmetry.

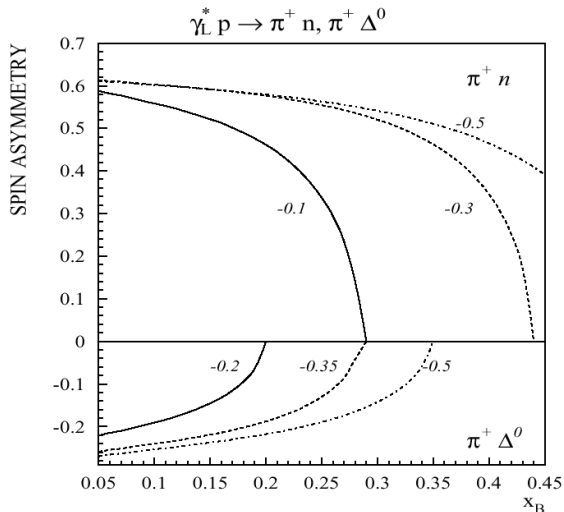


FIG. 3: Transverse single-spin asymmetry for the longitudinal electroproduction of  $\pi^+n$  and  $\pi^+\Delta^0$  at different values of  $t$  [indicated on the curves in  $\text{GeV}^2$ ]. The asymmetry drops to zero at the parallel kinematic limit, which is different for each  $t$  value, because the definition of  $P_y$  is ill-defined at this point. This figure is taken from Ref. [11].

It seems likely that a precocious factorization of the meson production amplitude into three parts – the overlap integral between the photon and pion wave functions, the hard interaction, and the GPD – will lead to a precocious scaling of  $A_L^\perp$  as a function of  $Q^2$  at

moderate  $Q^2 \sim 2 - 4 \text{ GeV}^2$  [9]. This precocious scaling arises from the fact that higher order corrections, which are expected to be significant at low  $Q^2$ , will likely cancel when one examines the ratio of two longitudinal observables. In contrast, the onset of scaling for the absolute cross section is only expected for much larger values of  $Q^2 > 10 \text{ GeV}^2$ .

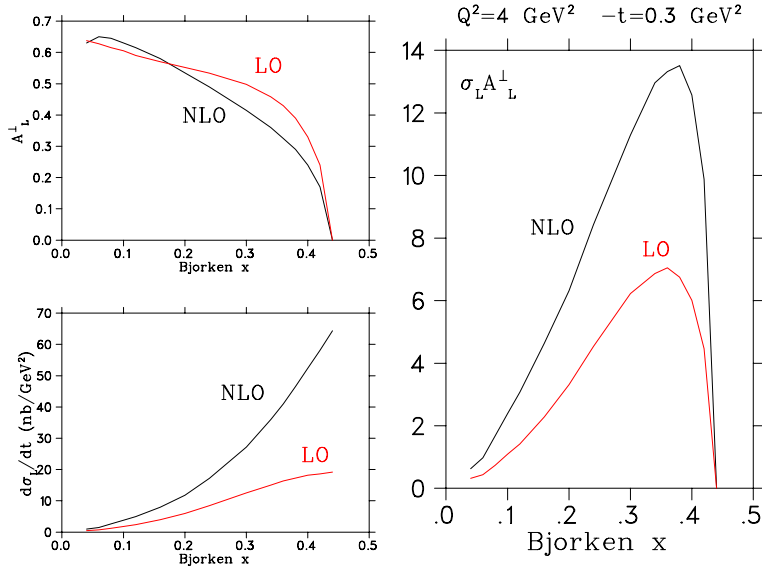


FIG. 4: Calculation of the longitudinal photon transverse nucleon spin asymmetry including twist-four corrections by A. Belitsky [12] at  $-t = 0.3 \text{ GeV}^2$ ,  $Q^2 = 4 \text{ GeV}^2$ . The red curves are the leading order calculation, while the black curves have twist-four power effects taken into account. While the cross section is very sensitive to these corrections, the transverse spin asymmetry is stable. The figure of merit  $\sigma_L A_L^\perp$  maximum at  $x_B = 0.37$  corresponds to particle angles and momenta similar to those proposed here.

This point is made clear in Fig. 4. This figure shows renormalon model calculations [12] of both the asymmetry and the longitudinal cross section at  $Q^2 = 4 \text{ GeV}^2$ . While the magnitude of the cross section changes significantly when taking into account the twist-four corrections,  $A_L^\perp$  is essentially insensitive to them and displays the expected precocious scaling. The relatively low value of  $Q^2$  for the expected onset of precocious scaling is important, because it will be experimentally accessible after the Jefferson Lab 12 GeV upgrade. This places  $A_L^\perp$  among the most important GPD measurements that can be made in the meson scalar. If precocious scaling cannot be experimentally demonstrated in the ratio of two purely longitudinal quantities, then it may not be possible to ever determine GPDs via hard exclusive meson production.

Refs. [3] and [11] also point out that the study of the transverse target single-spin asymmetry versus  $t$  is important for the reliable extraction of the pion form factor from electroproduction experiments (Fig. 2b). Investigations of hard exclusive  $\pi^+$  electroproduction using a pQCD factorization model [13, 14] find that at  $x_B = 0.3$  and  $-t = -t_{min}$ , the pion pole contributes about 80% of the longitudinal cross section. Since the longitudinal photon transverse single-spin asymmetry is an interference between pseudoscalar and pseudovector contributions, its measurement would help constrain the non-pole pseudovector contribution, and so assist the more reliable extraction of the pion form factor. The upper  $Q^2 = 6$  GeV<sup>2</sup> limit of the approved pion form factor measurements in the JLab 12 GeV program [15] is dictated primarily by the requirement  $-t_{min} < 0.2$  GeV<sup>2</sup>, to keep non-pion pole contributions to  $\sigma_L$  at an acceptable level [14]. Transverse target single-spin asymmetry studies versus  $t$  may eventually allow, with theoretical input, the use of somewhat larger  $-t$  data for pion form factor measurements, ultimately extending the  $Q^2$ -reach of pion form factor data acquired with JLab 12 GeV beam. Thus, measurements of the transverse single-spin asymmetry are a logical step in the support of the high priority (A rated) pion form factor program.

### C. Related Experimental Measurements

It has not yet been possible to perform an experiment to measure  $A_L^\perp$ . The conflicting experimental requirements of transversely polarized target, high luminosity, L-T separation, and closely controlled systematic uncertainty, make this an exceptionally challenging observable to measure.

The most closely related measurement, of the transverse single-spin asymmetry in exclusive  $\pi^+$  electroproduction without an L-T separation, was published by the HERMES Collaboration in 2010 [16]. Their data were obtained for average values of  $\langle x_B \rangle = 0.13$ ,  $\langle Q^2 \rangle = 2.38$  GeV<sup>2</sup> and  $\langle t' \rangle = -0.46$  GeV<sup>2</sup>, subject to the criterion  $W^2 > 10$  GeV<sup>2</sup>. The six Fourier amplitudes in terms of the azimuthal angles  $\phi$ ,  $\phi_s$  of the pion-momentum and proton-polarization vectors relative to the lepton scattering plane were determined. Of these, at leading twist only the  $\sin(\phi - \phi_s)_{UT}$  Fourier amplitude receives a contribution from longitudinal photons. If one assumes that longitudinal contributions dominate, these  $A_{UT}^{\sin(\phi - \phi_s)}$  values can be compared to GPD models for  $\tilde{E}$ ,  $\tilde{H}$ .

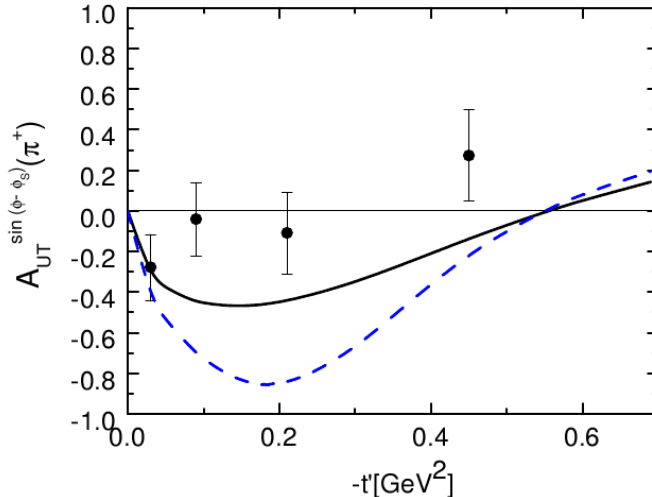


FIG. 5: Predictions by Goloskokov and Kroll for the  $\sin(\phi - \phi_s)$  moment of  $A_{UT}$  in the handbag approach, in comparison to the data from HERMES at  $Q^2 = 2.45 \text{ GeV}^2$ ,  $W = 3.99 \text{ GeV}$ . The independent variable is  $-t' = |t - t_{min}|$ . Dashed line: contribution from longitudinal photons only. Solid line: full calculation including both transverse and longitudinal photons. This figure is taken from Ref. [17].

However, as Goloskokov and Kroll indicate in their recent paper [17], a considerable share of the unseparated cross section measured by HERMES [16] is due to contributions from transversely polarized photons. In addition, there are contributions to  $A_{UT}^{\sin(\phi - \phi_s)}$  from the interference between two amplitudes, both for longitudinal photons, as well as transverse photons [18]. As indicated in Fig. 5, the contribution from transverse photons tends to make the asymmetry smaller. At the HERMES kinematics, the dilution caused by transverse photons is at least 50%. Because no factorization theorems exist for the exclusive production of  $\pi$  mesons by transverse photons, a simple interpretation of the HERMES  $A_{UT}^{\sin(\phi - \phi_s)}$  data in terms of GPDs is not possible.

**Jefferson Lab can make a unique contribution to studies of the  $\pi^-$  transverse spin asymmetry via the ability to take measurements at multiple beam energies and unambiguously isolate the longitudinal component of the asymmetry using a Rosenbluth separation.** In comparison to the HERMES measurement, the experiment proposed here will probe higher  $Q^2$  and  $x_B$ , and comparable values of  $t$ .

### D. Reasons why a Rosenbluth separation is required

Because transverse photon amplitudes are suppressed by  $1/Q$ , at very high  $Q^2$  it is safe to assume that all observed meson production is due to longitudinal photons. At the lower  $Q^2$  typical of the Jefferson Lab and HERMES programs, however, this is not the case. Handbag model calculations by Goloskokov and Kroll [19] for kinematics similar to those proposed here make this clear. The lower left panel of Fig. 6 shows their predictions for the cross section components in exclusive charged pion production. Although their calculations tend to underestimate the  $\sigma_L$  values measured in the JLab  $F_\pi - 2$  experiment [20], their model is in reasonable agreement with the unseparated cross sections [17]. They predict significant transverse contributions for JLab kinematics. A comparison of the unseparated asymmetry at  $-t = 0.3 \text{ GeV}^2$ ,  $x_B = 0.365$  in Fig. 6 with the separated longitudinal asymmetry at the same values of  $x_B$ ,  $-t$  in Fig. 4 indicates a substantial dilution of the unseparated asymmetry due to transverse photon contributions, similar to that observed in Fig. 5.

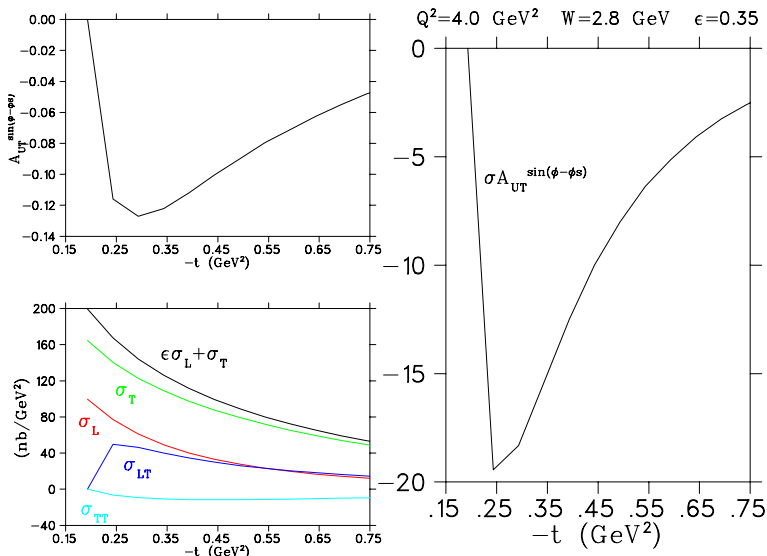


FIG. 6: Calculation of the cross section components and  $\sin(\phi - \phi_s)$  moment of the transverse nucleon spin asymmetry  $A_{UT}$  in the handbag approach by Goloskokov and Kroll [19] for kinematics similar to those in Fig. 4.  $x_B = 0.365$  for the kinematics in this figure.

At the amplitude level, Bartl and Majerotto [21] express the transversely-polarized nucleon cross section as

$$\frac{d\sigma_\perp}{dt} = \frac{P_y p_\pi W}{KM} [Im Y_1 + \epsilon \cos 2\phi Im Y_2 + 2\epsilon Im Y_3 + \sqrt{2\epsilon(1+\epsilon)} \cos \phi Im Y_4], \quad (7)$$

where  $P_y$  is the nucleon polarization component parallel to  $\hat{q} \times \hat{p}_p$ ,  $p_\pi, p_p$  are the outgoing pion and proton momenta in the virtual photon–nucleon center of mass frame,  $W$  is the invariant mass of the hadronic system,  $K = (W^2 - M^2)/2M$  is the so-called equivalent photon energy, and

$$Y_1 = h_+^N h_+^{F*} + h_-^N h_-^{F*} \quad (8)$$

$$Y_2 = h_-^N h_-^{F*} - h_+^N h_+^{F*} \quad (9)$$

$$Y_3 = h_0^N h_0^{F*} \quad (10)$$

$$Y_4 = h_0^N h_-^{F*} - h_0^F h_-^{N*} \quad (11)$$

The  $h$ 's are helicity amplitudes, where the superscripts  $F$  and  $N$  indicate baryon spin-flip and non-spin-flip amplitudes, respectively, and the subscripts 0, +, – indicate virtual photon polarizations longitudinal, parallel to the scattering plane, and perpendicular to the scattering plane. Thus, the desired term for study is  $Y_3$ , but at HERMES and Jefferson Lab energies one cannot ignore the contributions of  $Y_1$ ,  $Y_2$  and  $Y_4$  to the observed asymmetry.  $Y_1$  is especially problematic, because it can only be separated from  $Y_3$  with the use of a Rosenbluth separation. The transverse contributions to  $Y_1$  can be estimated with the use of a model [17, 22–24]. The transverse photon transverse nucleon spin asymmetry is generally expected to be smaller than the longitudinal photon transverse nucleon spin asymmetry, but nonzero for JLab kinematics, and so the experiment must be designed from the beginning to account for this contribution.

Looking more thoroughly at the contributions to the transverse nucleon spin asymmetry in the context of the (slightly modified) notation of Bartl and Majerotto [21], in the case of an unpolarized beam and unpolarized nucleon the virtual photoproduction cross section can be written as

$$\frac{d\sigma}{d\Omega} = \sigma_T + \epsilon \sigma_L + \epsilon \sigma_{TT} \cos 2\phi + \sqrt{\frac{1}{2}\epsilon(1 + \epsilon)} \sigma_{LT} \cos \phi, \quad (12)$$

where  $\sigma_T$ ,  $\sigma_L$ ,  $\sigma_{TT}$ , and  $\sigma_{LT}$  are the usual (modulo some factors of 2) transverse, longitudinal and interference cross sections and  $\phi$  is the azimuthal angle between the reaction plane and the scattering plane. These cross sections can be broken down into helicity amplitudes as

follows:

$$\sigma_T = \frac{p_\pi W}{KM} \frac{1}{2} (|h_+^N|^2 + |h_+^F|^2 + |h_-^N|^2 + |h_-^F|^2) \quad (13)$$

$$\sigma_L = \frac{p_\pi W}{KM} (|h_0^N|^2 + |h_0^F|^2) \quad (14)$$

$$\sigma_{TT} = \frac{p_\pi W}{KM} \frac{1}{2} (|h_-^N|^2 + |h_-^F|^2 - |h_+^N|^2 + |h_+^F|^2) \quad (15)$$

$$\sigma_{LT} = \frac{p_\pi W}{KM} 2Re (h_0^N h_-^{N*} + h_0^F h_-^{F*}). \quad (16)$$

For a polarized target, there is an additional contribution to the cross section:

$$\begin{aligned} \sigma_t = P_x & \left[ -\sqrt{2\epsilon(1+\epsilon)} \sin \phi \sigma_{LT}^x - \epsilon \sin 2\phi \sigma_{TT}^x \right] \\ & - P_y \left[ \sigma_{TT}^y + \epsilon \cos 2\phi \sigma_{TT'}^y + 2\epsilon \sigma_L^y + \sqrt{2\epsilon(1+\epsilon)} \cos \phi \sigma_{LT}^y \right] \\ & + P_z \left[ \epsilon \sin 2\phi \sigma_{TT}^z + \sqrt{2\epsilon(1+\epsilon)} \sin \phi \sigma_{LT}^z \right], \quad (17) \end{aligned}$$

where the various cross sections are given by:

$$\sigma_{LT}^x = \frac{p_\pi W}{KM} Im X_1 \quad (18)$$

$$\sigma_{TT}^x = \frac{p_\pi W}{KM} Im X_2 \quad (19)$$

$$\sigma_{TT}^y = \frac{p_\pi W}{KM} Im Y_1 \quad (20)$$

$$\sigma_{TT'}^y = \frac{p_\pi W}{KM} Im Y_2 \quad (21)$$

$$\sigma_L^y = \frac{p_\pi W}{KM} Im Y_3 \quad (22)$$

$$\sigma_{LT}^y = \frac{p_\pi W}{KM} Im Y_4 \quad (23)$$

$$\sigma_{TT}^z = \frac{p_\pi W}{KM} Im Z_2 \quad (24)$$

$$\sigma_{LT}^z = \frac{p_\pi W}{KM} Im Z_1. \quad (25)$$

The  $Y$  amplitudes have been defined earlier, and the  $X$  and  $Z$  amplitudes are made up of additional linear combinations of helicity amplitudes. The subscripts on each ‘‘cross section’’ denote whether they contain longitudinal amplitudes, transverse amplitudes, or both.

The  $x$ ,  $y$ , and  $z$  components of the target polarization are denoted  $P_x$ ,  $P_y$ , and  $P_z$ . In the co-ordinate system used here, the  $z$  direction is along the virtual photon direction ( $\vec{q}$ ), the  $y$ -axis is perpendicular to the hadron reaction plane (in the direction of  $\vec{q} \times \vec{p}_p$ ), and the  $x$  direction is given by  $\hat{y} \times \hat{z}$ .

In this discussion, we are interested in the transverse target asymmetries, so we will ignore the terms proportional to  $P_z$ . If we define  $\beta$  to be the azimuthal angle between the

component of the target polarization perpendicular to  $\vec{q}$  ( $P_\perp$ ) and the hadron reaction plane, we can re-express  $P_x$  and  $P_y$  as:

$$P_x = P_\perp \cos \beta \quad (26)$$

$$P_y = P_\perp \sin \beta \quad (27)$$

Note that if we set all the transverse amplitudes to zero in the above expressions for the unpolarized + polarized cross sections, we are left with

$$\frac{d\sigma}{d\Omega} = \epsilon \sigma_L - 2\epsilon \sigma_L^y P_\perp \sin \beta. \quad (28)$$

This is the basis for the exclusive pion transverse nucleon spin asymmetry defined in Ref.[8], which essentially extracts the ratio of  $\sigma_L^y$  to  $\sigma_L$ . For very large values of  $Q^2$ , transverse amplitudes should be small, so the above asymmetry can likely be extracted with no explicit L-T separation to isolate the longitudinal components. However, at the kinematics accessible at JLab one cannot assume that this will be the case, so we must take care to address the transverse contributions appropriately.

Experimentally, the angle between the target polarization and the reaction plane,  $\beta$ , and the angle between the scattering and reaction planes,  $\phi$ , are not independent. If the target polarization is at some angle,  $\phi_s$ , relative to the scattering plane, then  $\beta = \phi_s - \phi$ . For the experimental set-up that will be discussed here,  $\phi_s$  is relatively constant, so it will be useful to re-express the above cross sections in terms of  $\beta$  and  $\phi_s$ . The polarized nucleon cross section then becomes:

$$\begin{aligned} \sigma_t = & -P_\perp \sin \beta [\sigma_{TT}^y + 2\epsilon \sigma_L^y] \\ & - P_\perp \sin \beta [\epsilon(\cos 2\phi_s \cos 2\beta + \sin 2\phi_s \sin 2\beta) \sigma_{TT'}^y] \\ & - P_\perp \sin \beta \left[ \sqrt{2\epsilon(1+\epsilon)} (\cos \phi_s \cos \beta + \sin \phi_s \sin \beta) \sigma_{LT}^y \right] \\ & - P_\perp \cos \beta \left[ \sqrt{2\epsilon(1+\epsilon)} (\sin \phi_s \sin \beta - \cos \phi_s \cos \beta) \sigma_{LT}^x \right] \\ & - P_\perp \cos \beta [\epsilon(\sin 2\phi_s \sin 2\beta - \cos 2\phi_s \cos 2\beta) \sigma_{TT}^x]. \quad (29) \end{aligned}$$

From the above equation, it is clear that to extract the longitudinal photon transverse nucleon spin asymmetry it is necessary to first isolate the  $\sin \beta$  Fourier component of the polarized nucleon cross section. Once that has been accomplished, one must then separate the  $\sigma_L^y$  term from the  $\sigma_{TT}^y$  term via a Rosenbluth-type separation. This is what we propose to do in this experiment.

## II. EXPERIMENTAL METHOD

### A. High luminosity polarized Helium-3 target

We have been investigating various ways to reliably perform this measurement since our LOI in 2003 [25]. Recent advances in polarized target technology finally will make this measurement possible. We propose to perform this measurement using a transversely polarized  $^3\text{He}$  target to serve as an effective polarized neutron target. As described above, we must perform a L-T separation of the measured asymmetry in order to extract the (longitudinal photon) transverse nucleon single-spin asymmetry. High luminosity is essential for this experiment because the longitudinal cross section ( $\sigma_L$ ) is small for kinematics where the  $A_L^\perp$  is maximum and the cross section is large for kinematics where  $A_L^\perp = 0$ . We estimate that a luminosity of  $5 \times 10^{37} \text{ cm}^{-2}\text{s}^{-1}$  or higher is required to perform this measurement in a reasonable amount of time. This is more than a factor of 10 larger than the luminosity of the proposed upgraded Hall-A polarized  $^3\text{He}$  target. This target is not intended to replace that target for the  $A_1^n$  and  $d_2^n$  experiments, but should be seen as the development of a next generation of  $^3\text{He}$  target. The following section presents a short overview of target design; further details can be found in Appendix A.

Our polarized  $^3\text{He}$  target is based on a new approach developed by Prof. Bill Hersman's group at the University of New Hampshire. In this target, the critical polarizer components are positioned a comfortable distance ( $>$ three meters) away from the beam-target interaction point. The  $^3\text{He}$  gas is polarized in one or two large-capacity polarizers, compressed by a non-ferrous industrial-scale compressor and transported to the target cell. The cell is cryogenically cooled to increase its density during its interaction with the beam. The loop is closed by expanding the gas through a pressure-reducing orifice and directing it back to the polarizer(s) as shown in Fig. 7.

This arrangement has several advantages, both technical and operational. The pressure and temperature of the pumping cell can be optimized separately from the pressure and temperature of the target cell, each parameter selected to optimize its function. The system will be much less susceptible to magnetic field gradients. The target cell can be highly robust, fabricated from solid aluminum. Other components, especially those that may be considered less robust, can have built-in redundancy for fault-tolerance e.g. optionally incorporating a

second polarizer and/or a second compressor (see Fig. 7). We stipulate that the target cell can be designed to safely tolerate the full  $80 \mu\text{A}$  maximum beam current anticipated from the upgraded accelerator. The pressure of the target cell will be designed for pressures up to 3000 psi and the target cell will be cooled to 77 K wall temperature (which, when we account for beam heating, roughly doubles the density over a radiatively cooled cell) yielding 370 amagat density, which is  $0.5 \text{ g/cm}^2$  or  $1.0 \times 10^{23} \text{ atoms/cm}^2$  target thickness for a 10 cm long target. Combining this target thickness with the beam current yields a luminosity of  $5.0 \times 10^{37} \text{ e-}^3\text{He/cm}^2$ .

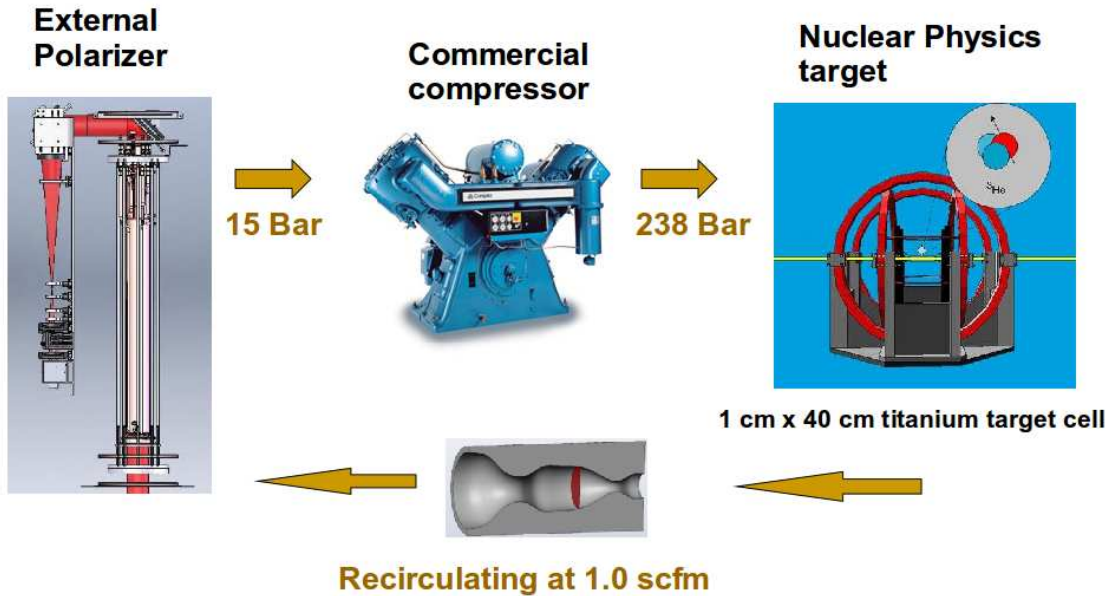


FIG. 7: The conceptual design of a high luminosity polarized  $^3\text{He}$  target for Hall-C. Note that for this experiment we will use a 10 cm aluminum target cell.

The large volume external polarizer is an existing spin-exchange optical pumping (SEOP) system using a hybrid alkali metal mix of K-Rb manufactured by Xemed [26]. It consists of a large 8.5 liter cylindrical glass vessel (10 cm diameter, 110 cm length) with thin optical window at one end. The glass cell is enclosed in a pressure vessel such that the external pressure can be adjusted to neutralize the differential pressure across the glassware. We

can therefore increase the polarizers  $^3\text{He}$  gas loading by choosing an operating pressure, up to 20 bar. The polarizer is divided into four thermal zones, two along the length of the barrel and two at the ends. The 1.1 meter long cylinder is mated to a two-zone oil-stabilized thermal system that is clamped around the glass cylinder. Two-thirds of its length farthest from the laser-entrance window, the gravitationally lower region of the cell, is maintained at higher temperature for achieving the desired alkali density for hybrid SEOP ( $\sim 250^\circ\text{C}$ ), while the upper one-third is maintained at a lower temperature to condense the alkali vapor back to a liquid. The champagne-bottle shaped end of the cell farthest from the laser is electrically heated to provide a continuous source of alkali vapor. The fourth zone, near the laser window, also has electrical heaters. The cell is surrounded by a 40 cm diameter, 120 cm long solenoid which provides a uniform magnetic field of 23 Gauss. A spectrally narrowed high power laser diode bar array consisting of 4 array of 12 bar stacks will provide 2.5 kW of laser power for optical pumping. Spin-up times of  $\sim 2.5$  hrs and polarizations of 50% have been achieved with a similar setup [27]. The whole polarizer has been designed to be a portable system, and software for fully automated process control has also been developed. Based on simulations of the SEOP process, it is expected that 60% polarization can be achieved with these polarizers.

The circulation system will consist of an a non-ferrous 3-stage diaphragm pump designed by Prof. Hersman's group and built by Fluitron Corporation [28], which is used to compress the polarized  $^3\text{He}$  to 200 atm pressure with minimal loss of polarization. The compressed polarized gas is then delivered to the target cell immersed in magnetic field at a flow rate of 25 standard liters per minute (SLPM). The proposed target cell will be 1 cm in diameter and 10 cm in length, machined from aluminum. An aluminum spherical-shell endcap of 1 cm diameter with thickness of  $500\ \mu\text{m}$  would reach 30% of the yield strength of aluminum at the operating pressure of 3000 psi, allowing a safety factor of 3. The target cell will be cryogenically cooled to 77K wall temperature in order to achieve the increased density that will help achieve the desired high luminosity. The polarized gas is then recirculated back into the polarizer via a pressure-reducing orifice. A magnetic holding field will be maintained around the target cell using large diameter Helmholtz coils. The polarization of the  $^3\text{He}$  gas will be monitored using NMR coils placed near the target cell. Low magnetic field NMR measurements of hyperpolarized gas through metal enclosures have been demonstrated before [29] and has recently been confirmed for titanium tubes. All sub-systems of the

proposed polarized  $^3\text{He}$  target, except for the aluminum target cell, have working prototypes.

For a reliable L–T separation, a short 10 cm target cell is required. The background from the target cell is minimal at the low epsilon (backward angle) kinematics, but are significant at the forward angle kinematics, as shown in Fig. 8. An empty dummy target cell will be used to measure the contributions from the target cell walls and will enable us to subtract away these contributions. Where possible, we will use thicker walls on the dummy target to minimize the beam time required to acquire these data. The rate estimated and projections have been performed assuming a 10 cm long cell with luminosity of  $5 \times 10^{37} \text{ cm}^{-2}\text{s}^{-1}$ .

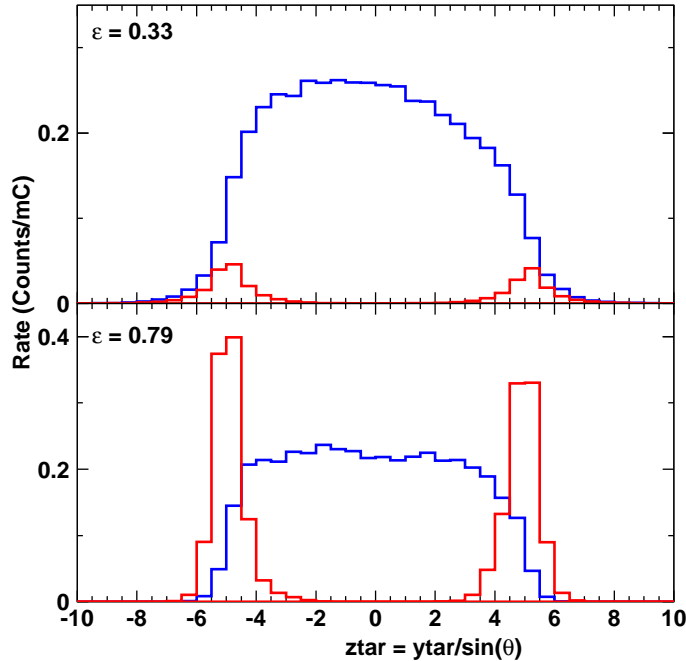


FIG. 8: Simulated  $z$ -target acceptance for the low and high  $\epsilon$  settings at  $Q^2 = 4.0 \text{ GeV}^2$ ,  $W = 2.6 \text{ GeV}$ . Background contributions expected from the  $500 \mu\text{m}$  thick aluminum walls of the target cell are shown in red. Acceptance cuts such as the “diamond cut” shown in Fig 11 have been applied.

A wide range of experiments have utilized polarized  $^3\text{He}$  as an effective neutron target over a wide range of kinematics. And over the past decades several authors have calculated the effective neutron polarizations in  $^3\text{He}$  using three-nucleon wave functions and various models of the  $N - N$  interaction [30]. These are now well established, and the error introduced by uncertainty in the wave functions are small.

Other nuclear effects which can influence the experimental asymmetry for a neutron bound inside  ${}^3\text{He}$  include, Fermi motion, off-shell effects, meson exchange currents, delta isobar contributions and  $\pi^-$  final state interactions. The exclusive nature of the process, the selected kinematics such as high  $Q^2$ , large recoil momentum and a complete coverage of the azimuthal angle  $\phi$  ensures that corrections due to these nuclear effects will be small and can be modeled effectively. For example, the recoil momentum is  $>450$  MeV/c for all settings proposed here, which minimizes Paul-blocking and  $\pi^-$  rescattering effects.

## B. Set-up and Kinematics

We intend to pursue this measurement in Hall C, using the HMS in coincidence with the SHMS using the proposed high luminosity polarized  ${}^3\text{He}$  target described above. While exclusive pion production measurements using CLAS-12 and a transversely polarized  ${}^1\text{H}$  target have been discussed previously [31], measurements utilizing the HMS–SHMS over a more limited kinematic range can be of great value because they allow the systematic error control necessary to perform a high quality Rosenbluth separation.

The reaction of interest is  ${}^3\text{He}(e, e'\pi^-)p + pp_{sp}$ . The measurement of the transverse single-spin asymmetry requires the detection of the  $\pi^-$  in non-parallel kinematics. It is the component of the target polarization parallel to  $\hat{q} \times \hat{p}_\pi$  that is important (Eqn. 7), and this direction is uniquely defined only in non-parallel kinematics. To accurately separate  $\sigma_L^y$  from  $\sigma_{TT}^y$  over a wide  $-t$  range, data will also be acquired to the left and right of  $\vec{q}$ . The acceptance of both spectrometers is sufficient to allow data to be acquired over  $0 < -t' < 0.4$  GeV<sup>2</sup>.

A Rosenbluth separation requires a minimum of two beam energies. To minimize the amplification in the systematic uncertainty, the  $\epsilon$  settings have been chosen to have as large  $\delta\epsilon$  as possible, while using only ‘standard 12 GeV’ 3 and 5-pass beam energies. The angle  $\beta$  between the target polarization and the reaction plane will be computed for each  $(Q^2, W, -t, \epsilon, \phi_{pq})$  bin and the  $\sigma_L$  and  $\sigma_L^y$  terms determined in a Rosenbluth-type separation.

Table I lists the proposed kinematic settings for this experiment. The ‘main setting’ at  $Q^2 = 4.0$  GeV<sup>2</sup>,  $W = 2.6$  GeV is near the maximum of the figure of merit shown in Fig. 4, to determine whether the dominance of the longitudinal contribution to the single spin asymmetry at intermediate  $Q^2$  is in fact a valid assumption. This choice of kinematics is

TABLE I: Near-parallel kinematic settings for this experiment. The  $\pi^-$  is detected in the SHMS and the scattered electron in the HMS. The linac gradient key is: A: 2.15 GeV/pass “12.0”.

$n(e, e'\pi^-)p$ Kinematic Settings						
$E_e$ (Pass #)	$E_{e'}$	$\theta_{e'}$	$\epsilon$	$\theta_q$	$p_\pi$	SHMS $\theta_{\pi q}$ Settings
(GeV)	(GeV)	(deg)		(deg)	(GeV/c)	(deg)
Main Setting $Q^2 = 4.00 \text{ GeV}^2$ , $W = 2.60 \text{ GeV}$ , $x_B = 0.40$ , $-t_{min} = 0.22$						
6.60 (3A)	1.345	39.21	0.333	-8.70	5.137	0, $+2.5^\circ$
10.92 (5A)	5.665	14.61	0.794	-14.72	5.137	0, $\pm 2.5^\circ$
Scaling Study $Q^2 = 3.00 \text{ GeV}^2$ , $W = 2.30 \text{ GeV}$ , $x_B = 0.40$ , $-t_{min} = 0.22$						
6.60 (3A)	2.659	23.86	0.645	-14.47	3.824	0, $\pm 2.5^\circ$
10.92 (5A)	6.979	11.39	0.891	-18.66	3.824	0, $\pm 2.5^\circ$
Non-pole Background $Q^2 = 4.00 \text{ GeV}^2$ , $W = 2.20 \text{ GeV}$ , $x_B = 0.50$ , $-t_{min} = 0.39$						
6.60 (3A)	2.366	29.31	0.572	-14.32	4.027	0, $\pm 2.5^\circ$
10.92 (5A)	6.686	13.44	0.868	-19.38	4.027	0, $\pm 2.5^\circ$

slightly lower from the  $W = 2.8 \text{ GeV}$  shown in Fig. 6 in order to avoid excessively large electron singles rates in the  $\pi^-$  spectrometer. A second set of measurements will be taken at the same  $x = 0.40$ , but lower  $Q^2 = 3.0 \text{ GeV}^2$ , to provide information on whether the longitudinal photon transverse target asymmetry scales versus  $Q^2$  as expected. The final set of measurements at  $Q^2 = 4.0 \text{ GeV}^2$ ,  $W = 2.2 \text{ GeV}$  is at significantly larger  $-t_{min} = 0.39$  (vs  $-t_{min} = 0.22 \text{ GeV}^2$  for the main setting) to provide information needed to constrain non-pion pole backgrounds to  $\sigma_L$ , helpful for the reliable extraction of the pion form factor from electroproduction data.

As part of the program to minimize the sources of systematic errors, the target polarization will be reversed periodically by reversing the magnetic field direction.

### C. Simulation of the Experiment - Acceptance

Simulations of this proposed measurement have been carried out using the standard Hall C Monte Carlo, SIMC. The Fermi motion of the neutron inside  $^3\text{He}$  was simulated using realistic neutron momentum distributions [32]. For these simulations, we have assumed that

the scattered electron is detected in the HMS, and the  $\pi^-$  in the SHMS. The simulations include radiative effects, effects from multiple scattering, and a pion electroproduction cross section model. In this case, the pion cross section used was a parameterization consistent with the separated cross sections extracted in the two pion form-factor experiments, E93-021 and E01-004 [33]. Exclusive  $\pi^\pm$  production data obtained in these experiments on  $^2\text{H}$  indicate that the  $R = \frac{\sigma_L}{\sigma_T}$  ratio is more favorable for  $\pi^-$  production, due to a  $t$ -dependent suppression of  $\sigma_T$ . The ratios assumed in our simulations are indicated in Fig. 9.

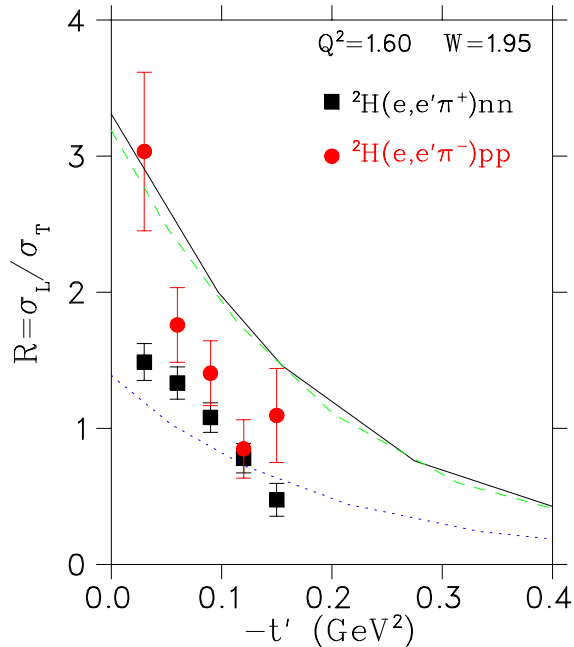


FIG. 9:  $R = \frac{\sigma_L}{\sigma_T}$  ratios on  $^2\text{H}$  from the first pion form factor experiment [34], in comparison to the ratios assumed in the simulations in this proposal at higher  $Q^2$ ,  $W$ . Solid line:  $Q^2 = 4.0 \text{ GeV}^2$ ,  $W = 2.6 \text{ GeV}$ . Dashed line:  $Q^2 = 3.0 \text{ GeV}^2$ ,  $W = 2.3 \text{ GeV}$ . Dotted line:  $Q^2 = 4.0 \text{ GeV}^2$ ,  $W = 2.2 \text{ GeV}$ .

Ideally, one would like full coverage of the angle between the target polarization vector and the reaction plane,  $\beta$  over the full range of  $t$ . The expected coverage for this experiment is shown in Fig. 10. No  $\sin \beta$  term was used to generate this distribution, hence the large numbers of simulated events in the vicinity of  $\pi/2$  and  $3\pi/2$  are due to the acceptance of the experimental configuration. This type of  $\beta$  coverage is well-suited to extracting the  $\sin \beta$  term of the polarized cross section given in Eqn. 29.

While the kinematics in Table I are for the nominal central values of  $Q^2$  and  $W$  (or  $x_B$ ),

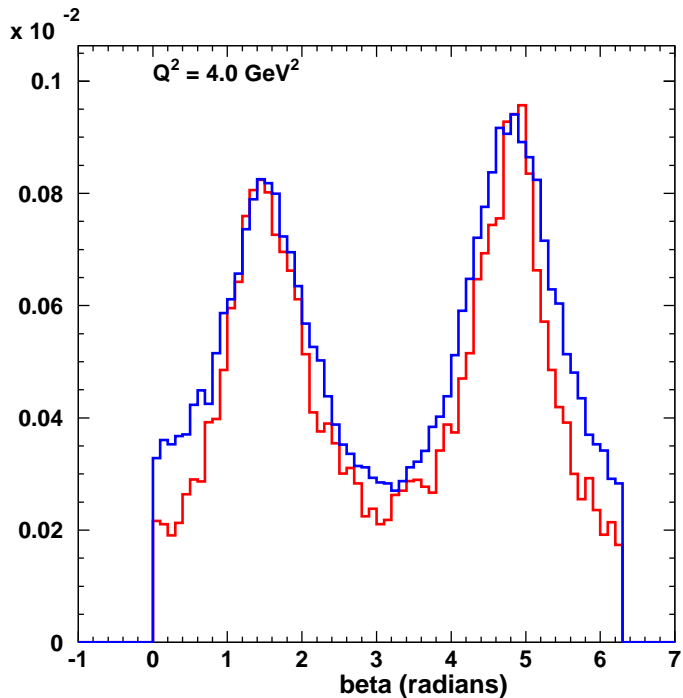


FIG. 10: Simulated distributions of the azimuthal angle of the target polarization with respect to the hadron reaction plane,  $\beta$ , summed over all SHMS angle settings at  $Q^2 = 4.0 \text{ GeV}^2$ ,  $W = 2.6 \text{ GeV}$ . The blue curves are the large  $\epsilon$  distributions and red curves are small  $\epsilon$ . These figures indicate full coverage in  $\beta$  at high and low  $\epsilon$  across the sampled  $t$  range.

the experimental acceptance allows a range of  $x_B$ ,  $Q^2$  and  $t$  to be sampled. This is desirable because the transverse spin asymmetry vanishes at  $-t_{min}$  (parallel kinematics) and grows rapidly as  $-t$  is increased. The kinematic coverage of the experiment is illustrated in Figs. 11 and 12. The coverage is sufficiently large to allow the data at each  $Q^2$  to be broken into several  $t$ -bins.

Fig. 13 shows the simulated missing mass spectra for both of the  $\epsilon$  settings at  $Q^2 = 4.0 \text{ GeV}^2$ ,  $W = 2.6 \text{ GeV}$ . The missing mass resolution is quite good, and should be more than adequate for separating the exclusive final state from multiple pion production and the residual  $\Delta$  final state. The contributions of  $2\pi$  states should be further suppressed by the high values of  $z$  used for this experiment.

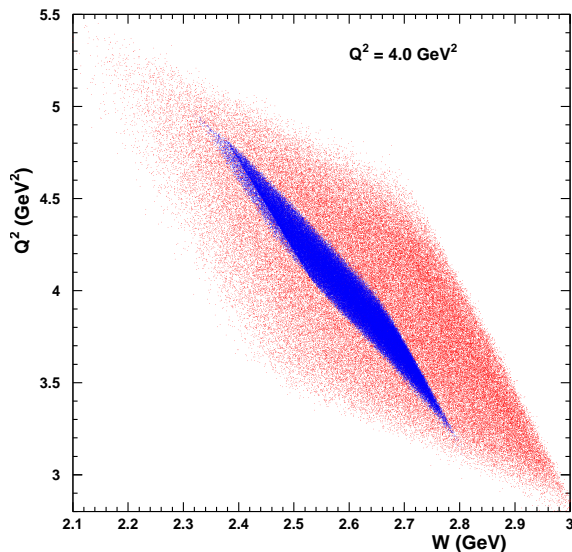


FIG. 11: Simulated experimental acceptance in  $Q^2$  and  $W$  for the high (blue) and low (red)  $\epsilon$  settings at  $Q^2 = 4.0 \text{ GeV}^2$ ,  $W = 2.6 \text{ GeV}$ . A “diamond” cut will be applied to match the kinematic coverages of the low and high  $\epsilon$  data.

#### D. Projected Real Event Rates

The SIMC simulations used for the above acceptance studies incorporate a cross section model [33] whose normalization has been checked against the available data. Thus, they can be used to reliably extract rate estimates. In preparing the estimates, we assume the use of 10 cm cryogenic targets and 80  $\mu\text{A}$  beam currents. Upon application of reasonable acceptance cuts and the phase-space matching cuts necessary for the L–T separation (Fig. 11), we estimate real coincidence rates of 2400(400) per hour for the  $Q^2 = 4.0 \text{ GeV}^2$ ,  $W = 2.6 \text{ GeV}$   $\epsilon = 0.79(0.33)$  settings; 13000(4800) per hour for the  $Q^2 = 3.0 \text{ GeV}^2$ ,  $W = 2.3 \text{ GeV}$   $\epsilon = 0.89(0.64)$  settings; and 4000(1200) per hour for the  $Q^2 = 4.0 \text{ GeV}^2$ ,  $W = 2.2 \text{ GeV}$   $\epsilon = 0.86(0.57)$  settings.

The quantity we ultimately wish to extract is a ratio of two longitudinal cross sections. As typically defined (i.e. Eqn. 6), the transverse target spin asymmetry as written in our notation corresponds to,

$$A_L^\perp = \frac{1}{P_\perp} \frac{2}{\pi} \frac{2\sigma_L^y}{\sigma_L}, \quad (30)$$

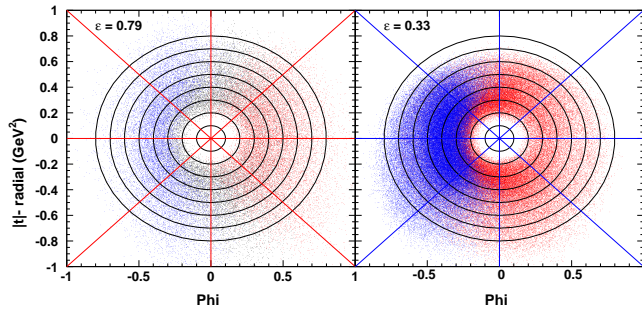


FIG. 12: Coverage of  $-t$  (radial coordinate) versus azimuthal angle  $\phi$  for the HMS+SHMS combination at  $Q^2 = 4.0 \text{ GeV}^2$ ,  $W = 2.6 \text{ GeV}$ . Each radial division corresponds to  $-t = 0.10 \text{ GeV}^2$ . Red, black and blue indicate the respective SHMS settings left and right of the  $q$ -vector. Cuts in  $Q^2$  and  $W$  have already been implemented to match the kinematic coverages of the low and high  $\epsilon$  data. The superposition of the SHMS settings allows good  $\phi$  coverage for the range of  $0.20 < -t < 0.60 \text{ GeV}^2$ .

where  $\sigma_L^y$  and  $\sigma_L$  were defined earlier in Sec I-D. To estimate the expected uncertainty in such a measurement, we assume the polarized target cross section has the following simplified form,

$$\sigma = \sigma_T + \epsilon\sigma_L - P_\perp \sin \beta (\sigma_T^y + \epsilon 2\sigma_L^y) . \quad (31)$$

The final uncertainty in any L–T separated cross section is sensitive to the ratio of the longitudinal to transverse cross sections ( $R = \frac{\sigma_L}{\sigma_T}$ ). For the calculations here, we assume an average value of 1.0, which is near the mid-point of the band shown in Fig. 9. The polarized longitudinal cross section is in general less well studied, so for now we assume the longitudinal response is the same size as the transverse ( $\sigma_L^y = \sigma_T^y$ ) for the two lowest  $-t$  bins and 1.5 times higher for the highest  $-t$  bin.

### E. Anticipated Singles Rates

All singles rate estimates assume the use of a 10 cm target cell, and the detection efficiencies listed in Table II, unless otherwise noted.

Anticipated rates in the SHMS and HMS were examined for  ${}^3\text{He}(e, e'\pi^-)$  data taking [35, 36], and are listed in the indicated columns of Table III. Since the SHMS is at negative

TABLE II: Anticipated HMS+SHMS detection efficiencies.

HMS tracking	0.95
SHMS tracking	0.95
pion absorption	0.95
pion decay (typical)	0.95
HMS: 5.9 msr acceptance for $\delta=-10\%$ to $+10\%$	0.9
SHMS: 3.5 msr acceptance for $\delta=-15\%$ to $+20\%$	0.9

polarity for  $\pi^-$  detection, there are large projected  $e^-$  singles rates for some settings. With a judicious choice of kinematics, one is able to keep the SHMS electron rates below 1 MHz in the worst cases. In order to keep the random coincidence rate to acceptable levels, an electron veto trigger with efficiency  $> 90\%$  will be necessary some SHMS settings. An atmospheric Argon–Neon Čerenkov detector, perhaps in combination with the lead–glass calorimeter can be used to form this trigger.

Identification and tracking of  $\pi^-$  will also be complicated by the high electron singles

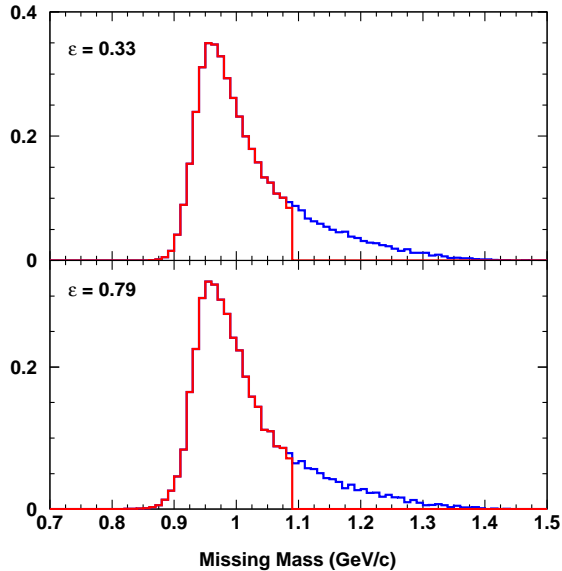


FIG. 13: Simulated missing mass distribution for the  ${}^3\text{He}(e, e\pi^-)p(pp)_{sp}$  reaction at  $Q^2=4.0 \text{ GeV}^2$ ,  $W = 2.6 \text{ GeV}$ , showing the cut region used for rate estimates.

rates in the SHMS. Assuming a  $\approx 100$  ns effective ADC gate for detectors that will be used to reject electrons, 1 MHz of electron singles implies that we will lose  $\approx 1 \text{ MHz} \times 100 \text{ ns} = 0.1$  of the  $\pi^-$  sample. Dedicated trigger studies will be needed to carefully determine the false  $\pi^-$  veto correction factor. The large singles rates will also result in reduced tracking efficiency. This was a key challenge in the analysis of  $\pi^-$  data from the first two pion form factor experiments, and the main issues are now understood. Accurate determination of the tracking efficiency at high rates depends to a large extent on a very clean trigger; “junk hits” in trigger scintillators from soft photons complicates the efficiency determination greatly. The quartz hodoscope in the SHMS, however, should not be as sensitive to these issues, so will be of much benefit in this case.

For the purpose of calculating online random coincidence rates, the SHMS trigger rate was taken as equal to the raw trigger rate, i.e. no distinguishing between pions, kaons and protons in the SHMS trigger. Assuming an online  $\pi^-$  and  $K^-$  rejection rate of 25:1, the HMS trigger rate was taken to be electrons plus  $(\pi^- + K^-)/25$ . The random coincidence rate is then given by (SHMS trigger rate)(HMS trigger rate) $\Delta t$ , where the coincidence resolving time was taken to be  $\Delta t=40$  nsec. In all cases, the resulting online real + random rates are well below the expected capability of the HMS+SHMS data acquisition system. Offline, the relevant resolving time is expected to be no worse than 2 nsec and the reals to randoms ratio for electron-pion coincidences after missing mass cuts will only be a few percent.

TABLE III: Projected SHMS and HMS rates with high luminosity polarized  $^3\text{He}$  target. The HMS+SHMS random coincidence rates assume a resolving time of 40 ns, a 25:1  $\pi^-$ ,  $K^-$  rejection ratio in the electron arm, and a 4:1  $e^-$  rejection ratio in the pion arm, thus corresponding to the online rate only; offline cuts will reduce this number to a few percent of the reals.

$\epsilon$	$I_{beam}$ ( $\mu\text{A}$ )	$\theta_{SHMS}$ (deg)	$\theta_{HMS}$ (deg)	SHMS Singles Rates			HMS Singles Rates			Random coinc.	Real coinc.
				(kHz)			(kHz)				
				$e^-$	$\pi^-$	$K^-$	$e^-$	$\pi^-$	$K^-$		
Main Setting $Q^2=4.00 \text{ GeV}^2$ , $W=2.60 \text{ GeV}$											
0.333	80	8.70	39.21	993	3.9	0.1	0.3	3.0	0.1	4	0.1
	80	11.20		171	0.7	0.1	0.3	3.0	0.1	1	0.1
0.794	80	14.72	14.61	9.7	0.8	0.1	9.1	0.3	0.1	1	3
	80	12.22		27	4.3	0.5	9.1	0.3	0.1	4	3
	80	17.22		3.1	0.2	0.1	9.1	0.3	0.1	1	3
Scaling Study $Q^2=3.00 \text{ GeV}^2$ , $W=2.30 \text{ GeV}$											
0.645	80	14.47	23.86	47	3.0	0.1	2.7	1.2	0.1	2	1.3
	80	11.97		119	10	0.5	2.7	1.2	0.1	5	1.3
	80	16.97		17	0.8	0.1	2.7	1.2	0.1	1	1.3
0.891	80	18.66	11.39	2.2	1.4	0.1	38	0.3	0.1	3	14
	80	16.16		4.8	4.9	0.5	38	0.3	0.1	10	14
	80	21.16		0.9	0.4	0.1	38	0.3	0.1	1	14
Non-pole Background $Q^2=4.00 \text{ GeV}^2$ , $W=2.20 \text{ GeV}$											
0.572	80	14.32	29.31	48	2.0	0.1	0.4	0.5	0.1	0.2	0.3
	80	11.82		135	7.4	0.3	0.4	0.5	0.1	1	0.3
	80	16.82		15	0.5	0.1	0.4	0.5	0.1	0.1	0.3
0.868	80	19.38	13.44	2.1	0.5	0.1	11	0.1	0.1	1	6
	80	16.88		4.8	2.2	0.2	11	0.1	0.1	3	6
	80	21.88		0.8	0.2	0.0	11	0.1	0.1	0.2	6

### III. PROJECTED UNCERTAINTIES AND BEAM TIME ESTIMATE

As with any L–T separation, the uncertainty in the longitudinal piece is subject to the usual  $1/\Delta\epsilon$  amplification. This means that we are the most sensitive to uncertainties that propagate randomly between  $\epsilon$  settings. There is a lot of experience in Hall C with L–T separations and their uncertainties. For the HMS–SOS set–up used in the first two pion form factor experiments, we were able to achieve uncorrelated (point-to-point) uncertainties of 0.7-1.2%,  $\epsilon$ -uncorrelated,  $t$ -correlated uncertainties of 1.7-2.0%, and correlated (scale) uncertainties of 2.8-3.5% [20]. For the SHMS–HMS, the uncorrelated errors are expected to be slightly improved from these values, due to the flatter SHMS  $y$ -target acceptance and lack of SOS-magnetic saturation effects. The simulated  $z$ -target acceptance for the ‘main’ kinematic setting, shown in Fig. 8, indicates that the full target is within the coincidence acceptance of the spectrometers, necessary for the careful control of target-related systematic uncertainties. Presently, we expect to run the high and low epsilon settings at similar beam currents. If we are required to run the high and low epsilon settings at significantly different beam currents, the point-to-point error may be somewhat degraded. In comparison to the 12 GeV pion form factor experiment [15], we have assumed a larger pt-to-pt acceptance uncertainty due to the longer target, as well as a larger pt-to-pt uncertainty in the Monte Carlo generator, as detailed in Table IV.

Two measurements at fixed  $(Q^2, W)$  and different values of  $\epsilon$  are needed in order to determine  $\sigma_L$ . Thus if  $\sigma_1 = \sigma_T + \epsilon_1\sigma_L$  and  $\sigma_2 = \sigma_T + \epsilon_2\sigma_L$  then

$$\sigma_L = \frac{1}{\epsilon_1 - \epsilon_2}(\sigma_1 - \sigma_2).$$

Assuming uncorrelated errors in the measurement of  $\sigma_1$  and  $\sigma_2$ , we obtain the intermediate expression

$$\frac{\Delta\sigma_L}{\sigma_L} = \frac{1}{(\epsilon_1 - \epsilon_2)} \frac{1}{\sigma_L} \sqrt{\Delta\sigma_1^2 + \Delta\sigma_2^2}.$$

and by defining  $r \equiv \sigma_T/\sigma_L$  and  $\Delta\sigma/\sigma \equiv \Delta\sigma_i/\sigma_i$  and assuming  $\Delta\sigma_1/\sigma_1 = \Delta\sigma_2/\sigma_2$ , then

$$\frac{\Delta\sigma_L}{\sigma_L} = \frac{1}{\epsilon_1 - \epsilon_2} \frac{\Delta\sigma}{\sigma} \sqrt{(r + \epsilon_1)^2 + (r + \epsilon_2)^2}.$$

This useful equation makes explicit the error amplification due to a limited  $\epsilon$  range and (potentially) large  $r$ . For the proposed experiment,  $r \leq 1$ , so a limited  $\epsilon$  lever arm is our primary source of uncorrelated error amplification, typically 3 here.

TABLE IV: Anticipated systematic errors based on our Fpi-2 (E01-004) experience. The uncorrelated errors between the low and high  $\epsilon$  settings are given in the first and second columns, and are magnified by  $1/\Delta\epsilon$  in the L-T separation. The bracketed quantities include our estimate of the partial cancellation of uncorrelated uncertainties when forming the ratio of two longitudinal cross sections ( $A_{\perp}^L$ ). The equivalent values determined in the Fpi-2 experiment are also listed at the bottom, for comparison.

Source	Type of systematic uncertainty		
	pt-to-pt (%)	$t$ -correlated (%)	scale (%)
Acceptance	0.7 (0.4)	0.4 (0.2)	1.0
Target Thickness		0.2	0.8
Beam Charge		0.2	0.5
HMS+SHMS Tracking	0.1	0.1	1.5
Coincidence Blocking		0.2	
PID		0.4	
$\pi$ Decay	0.03		0.5
$\pi$ Absorption		0.1	1.5
Monte Carlo Generator	0.4 (0.2)	1.0 (0.5)	0.5
Radiative Corrections	0.1	0.4	2.0
Offsets	0.4 (0.2)	1.0 (0.5)	
Quadrature Sum	0.8 (0.5)	1.6 (1.0)	3.3
Fpi-2 Values	0.9	1.9	3.5

In the end, we need to take the ratio of two longitudinal cross sections to obtain the asymmetry, and in taking that ratio, some of the systematic errors that are typically uncorrelated when one determines an *absolute* separated cross section become partially correlated when one takes their ratio. Based on our prior experience [37], uncorrelated uncertainties in the kinematics provide the dominant source of partial cancellation. For example, the high (low)  $\epsilon$  settings for  $\sigma_L^y$  and  $\sigma_L$  come from the same data sets, so the uncertainty from, e.g. the beam energy will be totally correlated at a given  $\epsilon$ , and hence reduce the  $1/\epsilon$  amplification.

$-t$	$\langle x_B \rangle$	Events( $\epsilon_{LO}$ )	Events( $\epsilon_{HI}$ )	$\frac{\delta\sigma_{LO}}{\sigma_{LO}}_{stat}$ (%)	$\frac{\delta\sigma_{HI}}{\sigma_{HI}}_{stat}$ (%)	$\frac{\delta\sigma_L}{\sigma_L}$ (%)	$\frac{\delta\sigma_T^y}{\sigma_T^y}$ (%)	$\frac{\delta A_{\perp}^L}{A_{\perp}^L}$ (%)
Main Setting $Q^2=4.00$ GeV <sup>2</sup> , $W=2.60$ GeV								
<0.40	0.385	122000	129000	0.29	0.28	8.8	9.8	8.6
0.40–0.60	0.405	60000	75000	0.41	0.36	8.9	10.6	9.3
>0.60	0.425	15700	25000	0.80	0.62	9.3	11.0	10.9
Scaling Study $Q^2=3.00$ GeV <sup>2</sup> , $W=2.30$ GeV								
<0.40	0.385	1000000	815000	0.10	0.11	18.4	18.7	16.9
0.40–0.60	0.400	365000	412000	0.17	0.16	18.4	19.1	17.3
>0.40	0.415	40000	92000	0.50	0.33	18.8	18.5	19.5
Non-pole Background $Q^2=4.00$ GeV <sup>2</sup> , $W=2.20$ GeV								
<0.55	0.48	182000	173000	0.23	0.24	15.0	16.1	14.6
0.55–0.75	0.52	128000	144000	0.28	0.26	15.0	16.5	14.9
>0.75	0.55	47000	67000	0.46	0.38	15.2	15.0	15.7

TABLE V: Columns 5,6: Projected statistical uncertainties on the unseparated cross sections in each  $-t$ -bin assuming the running times listed in Table VI. Columns 7,8: Total uncorrelated error on the longitudinal cross sections assuming 1.8% uncorrelated systematic errors. Column 9: Total projected uncertainty in the transverse target asymmetry including partial cancellation of uncorrelated systematic errors (1.2%) when forming the ratio. The above calculations assume  $r = \sigma_T/\sigma_L = 1$ , an asymmetry (or longitudinal ratio) as defined in Eqn. 30 of 0.5, and a <sup>3</sup>He target polarization of 65%.

Our estimates taking into account the partial cancellation of uncorrelated uncertainties are listed as the bracketed quantities in Table IV. These yield a total uncorrelated systematic uncertainty in the asymmetry ratio of 1.2%, while the contribution to the absolute cross section is 1.8%. Projected statistical and total uncorrelated errors for the proposed measurements are shown in Table V. The  $t$ -bins used in the table are only an example; finer  $t$ -binning might be possible, depending on actual experimental factors.

Projected uncertainties for the longitudinal photon transverse single spin asymmetry are shown in Fig. 14. Note that no uncertainty has been included for the target polarization. Assuming we can achieve 2% precision on this quantity, it is a minimal contribution to the uncertainty on the separated ratios. It is also worth mentioning that the unseparated

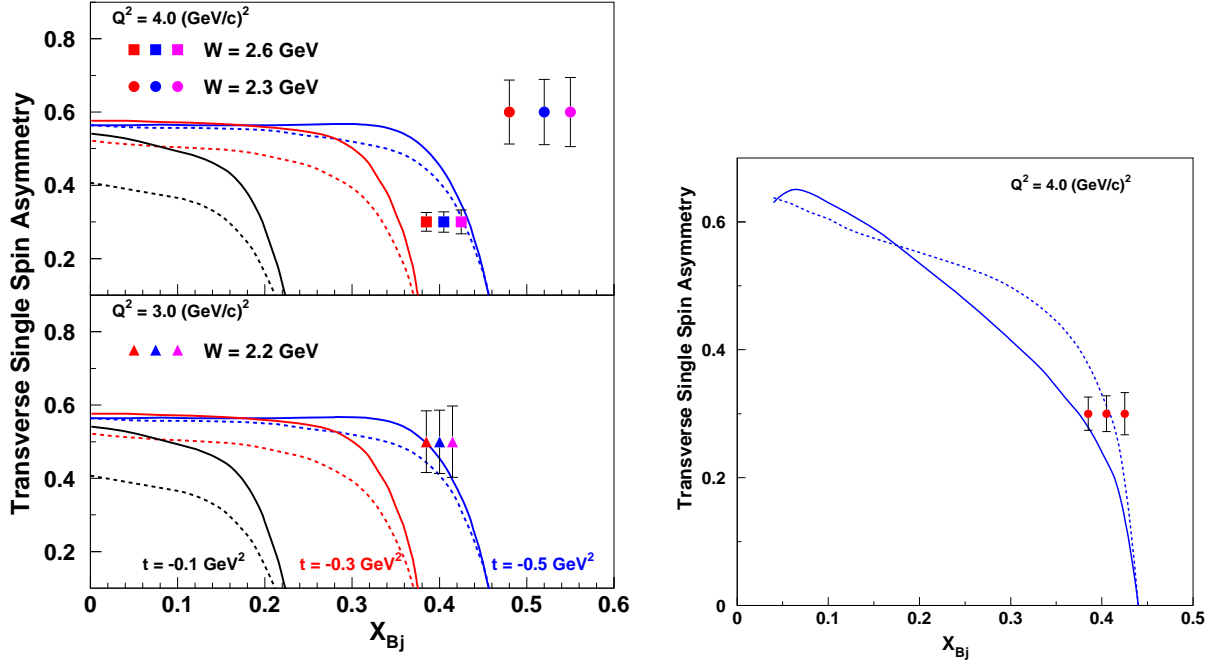


FIG. 14: Projected uncertainties for the  $L$ - $T$  separated transverse nucleon spin asymmetry for various assumed values of  $A_L^\perp$ . Each projected  $x_B$  point corresponds to the  $-t$  range noted in Table V. [Left:] The curves are predictions at various values of  $-t$  from Ref. [9] with asymptotic (solid) and Chernyak-Zhitnitsky (dashed) pion distribution amplitude. The “non-pole” setting points at  $W=2.3$  GeV extend past the limit of the theoretical curves because they are at higher  $-t$ , beyond the kinematic cutoff of the lower  $-t$  curves. [Right:] The curves are predictions at  $-t = 0.3$  GeV $^2$ ,  $Q^2=4$  GeV $^2$  from [12] at Leading-Order (dashed) and Next-to-Leading-Order (solid).

ratio can be measured with very good precision (on the order of 5–10% relative) since the uncorrelated errors for  $\sigma_L^y$  and  $\sigma_L$  are still rather small when combined in quadrature at a particular  $\epsilon$ .

Our beam time estimates are given in Table VI. As indicated in Fig. 8, target cell wall contributions are more significant in the high  $\epsilon$  settings. Based on our simulations, we allocate an additional 25% of high  $\epsilon$  running time for dummy target data collection, and 10% at low  $\epsilon$ . The total time needed to complete the experiment is 72.4 days (at 100% data collection efficiency).

TABLE VI: Projected running time to achieve the uncertainties in Table V. The number of  $^3\text{He}$  hours per setting is for all  $\theta_{\pi q}$  settings at high and medium  $\epsilon$  as listed in Table I. Dummy target times include both aluminum target for target cell wall subtraction, and nitrogen mock target cell as part of the calibrations. The overhead calculation assumes approximately one day per week will be needed for target duties, kinematic changes, etc.

$Q^2$ (GeV $^2$ )	$W$ (GeV)	$\epsilon$	$^3\text{He}$ Data Taking (Hours)	Dummy Target (Hours)	Overhead (Hours)	Total
4.0	2.6	0.333	480	48	75	603
		0.794	96	24	17	137
3.0	2.3	0.645	288	29	45	362
		0.891	96	24	17	137
4.0	2.2	0.572	288	29	45	362
		0.868	96	24	17	137
Subtotals			1344	178	216	1738

Grand Total: 1738 hours (72.4 days)

#### IV. SUMMARY

The transverse single-spin asymmetry in the exclusive  $\vec{n}(e, e'\pi^-)p$  reaction has been noted as being especially sensitive to the spin-flip generalized parton distribution (GPD)  $\tilde{E}$ . Factorization studies have indicated that precocious scaling is likely to set in at moderate  $Q^2 \sim 2 - 4 \text{ GeV}^2$ , as opposed to the absolute cross section, where scaling is not expected until  $Q^2 > 10 \text{ GeV}^2$ . Furthermore, this observable has been noted as being important for the reliable extraction of the charged pion form factor from pion electroproduction. Two crucial aspects of our experiment, which distinguish it from other previous or proposed measurements are the Rosenbluth L–T separation with controlled systematic uncertainties, and a new, externally polarized, continuous flow, high luminosity  $^3\text{He}$  target based on a large volume polarizer and compressor developed at the University of New Hampshire. Unlike other ongoing or proposed experiments, where the dominance of the longitudinal contribution to the spin asymmetry at intermediate  $Q^2$  is simply assumed, we intend to demonstrate

whether this is in fact the case. Experimental data will be the final judge of whether soft physics contributions cancel sufficiently well in the asymmetry ratio to allow the GPD mechanism to be observable at JLab energies. We have designed our experiment to remove the contribution of competing physics backgrounds to the greatest extent possible, through the L–T separation, and the exclusive measurement. Thus, the magnitude of the observed asymmetry and its kinematic dependence should be a good test of whether the precocious scaling expectations of the GPD formalism will be ultimately realized at JLab energies. Our measurement will also help to constrain longitudinal backgrounds possibly complicating the extraction of the pion form factor from electroproduction experiment data, with the aim of eventually extending the kinematic range over which reliable data can be acquired from electroproduction data.

- 
- [1] M. Diehl, Contribution to the eRHIC White Paper, arXiv:hep-ph/0010200.
  - [2] J.C. Collins, L. Frankfurt, M. Strikman, Phys. Rev. D **56** (1997) 2982.
  - [3] K. Goeke, M.V. Polyakov, M. Vanderhaeghen, Prog. Part. Nucl. Phys. **47** (2001) 401-515.
  - [4] A.V. Radyushkin, arXiv:hep-ph/0101225.
  - [5] A.W. Thomas, W. Weise, “The Structure of the Nucleon”, J. Wiley-VCH, 2001.
  - [6] R.E. Marshak, Riazuddin, C.P. Ryan, “Theory of Weak Interactions in Particle Physics”, J. Wiley, 1969.
  - [7] M. Penttinen, M.V. Polyakov, K. Goeke, Phys. Rev. C **62** (2000) 014024 1-11.
  - [8] A.V. Belitsky, D. Mueller, Phys. Lett. **B 513** (2001) 349-360.
  - [9] L.L. Frankfurt, P.V. Pobylitsa, M.V. Polyakov, M. Strikman, Phys. Rev. D **60** (1999) 014010 1-11.
  - [10] M. Vanderhaeghen, P.A.M. Guichon, M. Guidal, Phys. Rev. D **60** (1999) 094017 1-28.
  - [11] L.L. Frankfurt, M.V. Polyakov, M. Strikman, M. Vanderhaeghen, Phys. Rev. Lett. **84** (2000) 2589-2592.
  - [12] A.V. Belitsky, CIPANP 2003 proceedings. arXiv: hep-ph/0307256.
  - [13] L. Mankiewicz, G. Piller, A. Radyushkin, Eur. Phys. J. **C 10** (1999) 307-312.
  - [14] C.E. Carlson, J. Milana, Phys. Rev. Lett. **65** (1990) 1717.
  - [15] E12-06-101, “Measurement of the Charged Pion Form Factor to High  $Q^2$ ”, G.M. Huber, D.

Gaskell, spokespersons.

- [16] A. Airapetian, Phys. Lett. **B 682** (2010) 345-350, arXiv:0907.2596 [hep-ex].
- [17] S. V. Goloskokov and P. Kroll, Eur. Phys. J. C **65**, 137 (2010), arXiv:0906.0460 [hep-ph].
- [18] M. Diehl, S. Sapeta, Eur. Phys. J. C **41** (2005) 515, arXiv:hep-ph/0503023.
- [19] S. V. Goloskokov and P. Kroll, private communications 2009-12.
- [20] H.P. Blok, et al., Phys. Rev. C **78** (2008) 045202.
- [21] A. Bartl, W. Majerotto, Nucl. Phys. **B62** (1973) 267-285.
- [22] M. Vanderhaeghen, M. Guidal, J.-M. Laget, Phys. Rev. C **57** (1998) 1454.
- [23] C. Bechler, D. Mueller, arXiv:0906.2571[hep-ph].
- [24] M.M. Kasulov, U. Mosel, Phys. Rev. C **80** (2009) 023202.
- [25] LOI 03-104, “The Longitudinal Photon, Transverse Nucleon, Single-Spin Asymmetry in Exclusive Pion Electroproduction”, D. Gaskell, G.M. Huber, G. Warren.
- [26] E. Babcock *et al.* Phys Rev Lett, **91**, (2003) 123003.
- [27] E. Babcock *et al.* Phys Rev Lett, **96**, (2006) 083003.
- [28] Fluitron Corporation, 900 Louis Drive Warminster, PA 18974.  
<http://www.pressureproductsindustries.com>
- [29] C.-H. Tseng *et al.*, Phys. Rev. Lett. **81**, (1998) 3785.
- [30] J. L. Friar *et al.*, Phys. Rev. C **42**, (1990) 2310; C. Ciofi degli Atti, and S. Scopetta, Phys. Lett. **B404**, (1997) 223; R.W. Schulze and P.U. Sauer, Phys. Rev. **C56** (1997) 2293; F. Bissey, A.W. Thomas, and I.R. Afnan, Phys. Rev. **C64**, (2001) 024004.
- [31] pCDR for the Science and Experimental Equipment for the 12 GeV Upgrade of CEBAF, June, 2004.  
V. Burkert *et al.*, PAC18 Review of the Science Driving the 12 GeV Upgrade, July, 2000.
- [32] R. B. Wiringa, private communication
- [33] T. Horn, parameterization of  $p(e, e'\pi^+)n$  separated cross sections, 2006.
- [34] G.M. Huber, E93-021 “nearly final”  $^2\text{H}$  results, April, 2012.
- [35] wiser.f by Steve Rock. Wiser fit of  $p^\pm, \pi^\pm, K^\pm$  cross sections  $5 < E < 19$  GeV and  $5 < \theta < 50^\circ$ .
- [36] rates.f by Eric Christy. Fit of electron elastic and inelastic scattering cross sections.
- [37] D.J. Gaskell, Ph.D. Thesis, “Longitudinal Electroproduction of Charged Pions from Hydrogen, Deuterium, and Helium-3”, Oregon State University, 2001.

## APPENDIX A: FURTHER DETAILS ON THE HIGH LUMINOSITY POLARIZED $^3\text{He}$ TARGET

### 1. Challenges and opportunities for an ex-situ configuration

Our polarized  $^3\text{He}$  target is based on a new approach where the critical polarizer components are positioned a comfortable distance ( $>$ three meters) away from the beam-target interaction point. The  $^3\text{He}$  gas is polarized in one or two large-capacity polarizers, compressed by a non-ferrous industrial-scale compressor and transported to the target cell. The cell is cryogenically cooled to increase its density during its interaction with the beam. The loop is closed by expanding the gas through a pressure-reducing orifice and directing it back to the polarizer(s). (Fig. 15)

This conceptual arrangement has several advantages, both technical and operational. The pressure and temperature of the pumping cell can be optimized separately from the pressure and temperature of the target cell, each parameter selected to optimize its function. The system will be much less susceptible to magnetic field gradients. The target cell can be highly robust, fabricated of solid metal (aluminum, titanium, or beryllium as needed). Other components, especially those that may be considered less robust can have built-in redundancy for fault-tolerance e.g. optionally incorporating a second polarizer and/or a second compressor.

We estimate the potential figure of merit, luminosity times polarization-squared, of our proposed  $^3\text{He}$  target system. Beginning with luminosity, we stipulate that our target cell can be designed to safely tolerate the full  $80\ \mu\text{A}$  maximum beam current anticipated from the upgraded accelerator, a rate of  $5.0 \times 10^{14}$  electrons/sec. The pressure of the target cell can be freely chosen: we design for pressures up to 3000 psi. We cool the target to 77 K wall temperature (which, when we account for beam heating, roughly doubles the density over a radiatively cooled cell) yielding 370 amagat density, which is  $0.5\ \text{g}/\text{cm}^2$  or  $1.0 \times 10^{23}$  atoms/ $\text{cm}^2$  target thickness for a 10 cm long target. Combining this target thickness with the beam current yields a luminosity of  $5.0 \times 10^{37}$  e- $^3\text{He}/\text{cm}^2$ . The luminosity of the existing 40cm long Hall A target, which allows  $15\ \mu\text{A}$  on a target with density of 10 amagat is lower by a factor of almost 40.

We next consider the potential polarization rate of our system. The pressure in our

polarizer is a design variable set by the certified working pressure of the vessel. We choose to design our vessel for certification at a minimum of 300psi. (In fact, we will seek certification at the highest practical pressure for an additional margin.) Each polarizer illuminates a volume of 8.5 liter, which represents 90 STP liters of  $^3\text{He}$  at a density of 10.6 amagat, 4 moles. This is slightly more than 50 times the typical 1.7 STP liter  $^3\text{He}$  gas volume illuminated in the 3-inch diameter glass sphere by the present Hall A target. Assuming beam depolarization dominates the depolarization losses for both systems, we conclude that our proposed system will provide a factor of fifty higher polarization rates, as well as a factor of fifty greater depolarization rates, leaving the ratio of these two parameters for the new system comparable to that of the existing Hall A target. Consequently, the polarization of our proposed target system for Hall C is expected to be 65%, equal to that of the existing Hall A target but at 50 times the luminosity. If a second polarizer is incorporated into the system for fault tolerance and additional polarizing capacity, then the polarization should be higher.

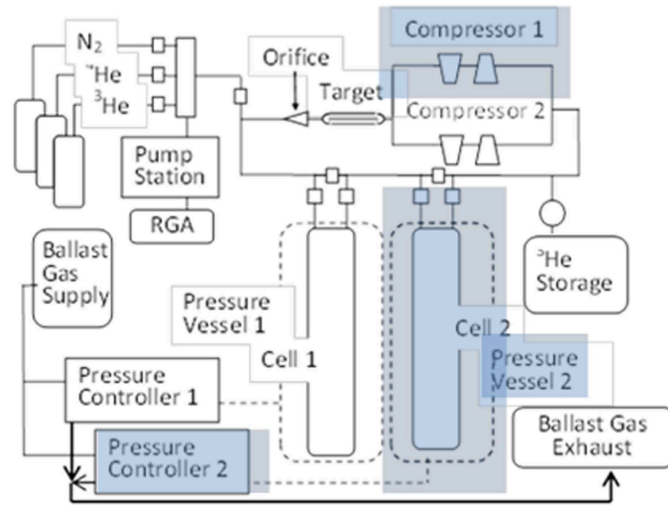


FIG. 15: Schematic of a fault-tolerant high-pressure electron target system. While this project utilizes just one polarizer and one compressor, the system can be expanded by adding redundant components (with the blue background) which can increase capacity and improve fault-tolerance.

## 2. History of Xemed's large-scale polarizer of $^3\text{He}$

Hybrid Spin Exchange Optical Pumping (HSEOP), originated in 1997 independently at Princeton and New Hampshire, uses a mixture of rubidium (Rb) and potassium (K) as the alkali vapor intermediary. Because K-He spin-exchange is less “lossy” than Rb-He requiring fewer replacement photons, HSEOP can reach higher efficiencies by using high alkali densities at higher temperatures, reducing the “spin-up time” from roughly a day to just a few hours. The University of New Hampshire and Xemed demonstrated unprecedented polarized  $^3\text{He}$  spin-up rates using this first fully scalable HSEOP polarizer of  $^3\text{He}$ . Optical pumping was provided by two diode laser stacks operating at 800-1000 watts each of broadband (2.5 nm) radiation centered at 794.7 nm. Xemed made three types of experimental studies of this system: the total spin exchange rate, near-asymptotic polarization, and wall relaxation ( $T_1$ ). We measured the spin-exchange using a “polarization zero-crossing” method, in which we reverse the polarization of the laser by rotating a quarter waveplate in the laser by  $90^\circ$ . At zero-crossing the polarization rate of change is equal to the bulk average spin-exchange in the cell. Since there is no polarization loss, the measured spin-exchange depends only on the cell geometry, laser power, and temperature profile. Therefore, the polarization zero-crossing measurement is effective for parametric studies of geometric and thermal configurations of the system, regardless of the quality of the cell. The near-asymptotic polarization measurement consists of running the polarizer for a period of two hours or more to capture the trend towards asymptotic polarization. Wall relaxation (i.e.  $T_1$ ) measurements consist of recording the polarization overnight after the laser and heaters are turned off.

The most comprehensive set of experiments occurred in Feb 2009 with a Pyrex cell and July 2009 with an aluminosilicate cell. The three polarization reversal measurements demonstrate a spin-up rate of 20% per hour on a cell containing almost 50 STP liters of gas, roughly two moles. This volumetric spin-up rate of 0.4 mole per hour is by far the highest ever achieved. The near asymptotic run shows an actual polarization greater than 30% and trending to 50%. This was accomplished using a cell with  $T_1$  of only 11 hours.

### **3. Current status: Zeppelin v3.0**

We are presently commissioning our next-generation large-scale  $^3\text{He}$  polarizer, Zeppelin 3.0 (see Fig. 16). A key improvement of this polarizer is the incorporation of a 2.5kW spectrally-narrowed laser, replacing the broadband laser. This laser is a configuration that we invented in 2007 in which internal cavity feedback on an unlimited number of bars in a laser diode stack is established using a stepped-mirror to redirect the beam to a diffraction grating in Littrow configuration. Narrow-band pumping is important for two reasons: 1) it eliminates off-resonant depolarization that occurs with broadband optical pumping of  $^3\text{He}$  and 2) it decreases the heating load associated with a given level of optical pumping. The other subsystems have been significantly upgraded and incorporated into a single package that can be easily relocated without disassembling. The oven system has been redesigned to provide more mechanical stability and ease of assembly; the electrical system uses 60 amps, 3 phase, 208 VAC power with appropriate circuit breakers, solid state relays, fuses, and emergency shut-down switch to allow for fail-safe operation and automation; the gas handling system uses a high-purity integrated gas panel. Control of the polarizer uses the .NET environment with a layered software system in C# and LabView, driving a National Instruments CompactRIO control system. We have designed and assembled a custom frame that houses all components, assures laser safety, and meets the robustness requirements of moving the polarizer between locations. On April 20, 2012 we observed our first polarization signal from NMR FID on polarized  $^3\text{He}$  with the new system.

### **4. Status of Non-ferrous Circulation System**

The electron-beam target technology that we proposed requires pressure changes from 300 psi to 3000 psi at flow rates of 25 standard liters per minute (SLPM), conditions which exceed the capabilities of existing technology by over three orders of magnitude. To address these requirements we worked with Fluitron Corporation of Warminster, PA to design the first stage of a two-stage a non-magnetic diaphragm compressor similar to compressors used for compression of high purity industrial gases. We follow other groups by selecting non-magnetic materials with minimal iron and nickel content: the compressor head is made from 6AL4V titanium, the wetted diaphragm is phosphor bronze, and the check valve assemblies



FIG. 16: Zeppelin 3.0 Polarizer. Top Row (left to right): Polarization cell after bakeout and alkali distillation; cell loaded into two zone heat exchanger; insulated cartridge repaired for loading; Middle Row (left to right): Bottom view of cartridge being loaded into cell; top flange of pressure vessel with oil heating hoses, instrumentation feedthroughs, and shielded laser light path; oil heating, gas handling, and laser power/cooling systems; polarizer electrical controls box; Bottom: cell being loaded into the pressure vessel; system prepared for cell/solenoid/pressure vessel installation; complete polarizer with cell assembly lifted into one operating position.

consist of beryllium copper springs with PEEK poppet heads. Prior to delivery of our pumps we had the manufacturer perform our required tests of their flow characteristics with  $^4\text{He}$ .

The resulting flow characteristic of the high pressure stages appears in Fig. 17. The compressor exceeded our design specification of 15 liter with 150 psig suction and 1000 psig

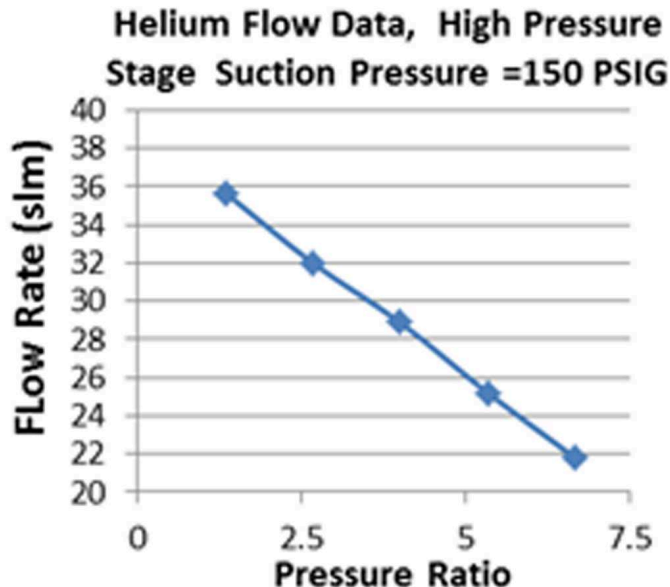


FIG. 17: Tests of an industrial-scale diaphragm compressor assembled with non-ferrous materials meets our requirements for flow, achieving 22 SLPM at 1000 psi output pressure.

discharge. The single stage can delivery adequate flow to meet the demands of the polarizer. Based on discussions with the manufacturer, we know that slight modifications to this pump will allow it to be operated with suction pressure up to 300 psig with outlet pressures up to 3000 psig. Both the high pressure and low pressure stages were operated for periods exceeding 80 hours, disassembled and inspected for wear, and then reassembled and tested again. The two titanium diaphragm pumps have been incorporated into a flow test facility for tests of  $^3\text{He}$  depolarization.

To maintain a magnetic holding field for the  $^3\text{He}$  and for performing NMR on the components within the flow loop, we need to generate a uniform magnetic field over a volume about one meter in diameter. We repurposed two existing large diameter coil pairs (Fig. 18); the inner pair is 1.8 m in diameter while the outer pair is 1.2 m in diameter. We developed a numerical model that guided our optimization of coil separation and current. The two large coils each have their own power supply capable of delivering 40 amps, while a single supply is used to power the outer coil pair up to 35 amps. We demonstrated that this system can generate uniform fields up to 75 gauss. By mapping the field along the axis, we found that it is uniform to 1 part in 1000 over a 30 cm volume.

To evaluate performance of proposed target and analyzer systems, we created a mock-up flow loop that allowed us to make meaningful measurements concerning polarization losses during the cycling of polarized helium between a polarizer into a holding reservoir or large neutron analyzer. Characterizing the polarization losses will be accomplished using an NMR coil looped around one of the reservoirs.



FIG. 18: Large 1.8 m magnetic field coils achieve 75 Gauss with  $10^{-3}$  uniformity.

The high pressure of the polarizer is throttled down to the analyzer pressure by two precision sapphire “Vee” orifices that we obtained from Bird Precision Orifices that are .002” and .003” in diameter; these orifices can be opened independently using manual titanium valves. We chose these orifices over other throttling techniques (e.g. capillary tube or needle valves) because they dissipate the pressure in a series of oblique shock waves downstream of the opening rather than by viscous interaction with the surrounding surfaces. We did initially consider the use of converging-diverging deLaval nozzles to minimize recirculation that occurs downstream of the orifice. However, the literature indicated that at the small size scale and high density we are considering, the pressure dissipation is dominated by viscosity, defeating the original intent of the converging-diverging geometry.

The high pressure stage may be bypassed and the gas circulated using the low pressure stage alone. This serves two purposes. First, it allows us to evaluate polarization losses that occur during evacuation of the analyzer into the reservoir. Second it allows us to circulate polarized gas with no significant pressure drop, to evaluate the intrinsic polarization losses associated with flow through the system.

We had previously demonstrated low magnetic field NMR measurements of hyperpolarized gas through metal enclosures due to the large skin depth at kHz RF frequencies. We recently confirmed this fact by showing that gas polarization measurements can be taken through a titanium tube similar to the transfer lines we propose. Titanium has a low electric conductivity, further increasing skin depth and allowing signal transmission and reception through the tube wall. We were able to test this concept using polarized natural xenon, which was produced by our XeBox-E10 medical polarizer. This test used an 8 inch section of 0.5" OD x 0.4" ID titanium tubing which was plugged on either end with rubber stoppers, one with a glass feed-through tube. Our NMR was a coil that was wrapped around the titanium tube. The tube was evacuated to 1 torr and then filled with a mixture of polarized natural xenon and nitrogen from a Tedlar bag. To unambiguously estimate the flip angle, we measured the polarization decay at three different drive signal amplitudes (1 Vpp, 0.25 Vpp, and 0.05 Vpp) and fit the profile. The results appear in Fig. 19. We see that the measured T1 improves at low drive voltages, and that longest T1 was 440 sec.

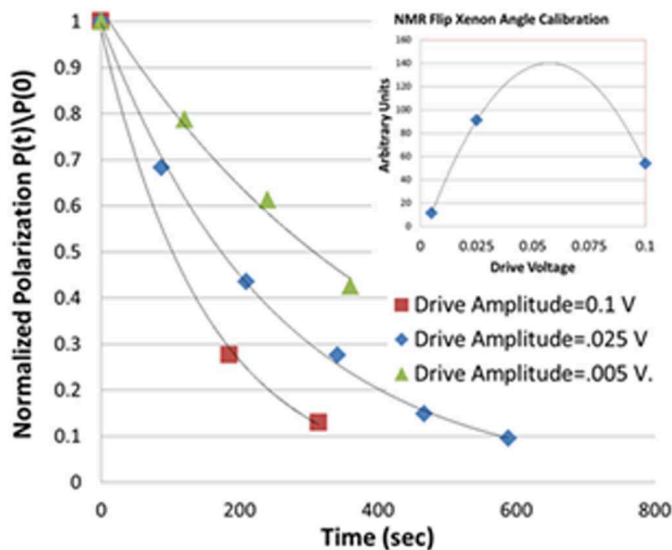


FIG. 19: NMR signal measurements as a function of time for three flip angles.  $S/V = 3.9$

## 5. Design and optimize the high-pressure target cell, including cryogenics

The experimental figure of merit for statistical determination of any polarized  $^3\text{He}$  asymmetry observable is the polarization-squared times the luminosity. Higher luminosity, however, leads to higher relaxation rates, reducing the polarization. Consequently, the figure of merit will peak at a value of the luminosity where the average polarized  $^3\text{He}$  spin-up rate is balanced by the beam-induced depolarization rate. It can be shown that the  $P^2 I$  peak occurs where the polarization of the system is reduced to half-maximum. With the above system specifications, we expect spin up rates from each  $^3\text{He}$  polarizer of one mole  $^3\text{He}$  per hour (25% per hour on four moles). Given a beam depolarization constant, measured in Hall-A, of  $10^{-39}$  hours per mole of gas times the luminosity, we project a peak in the figure of merit of our two-mole-per-hour dual polarizer system to occur at a luminosity of  $2 \times 10^{39}$  with polarization 35%. Since we plan to support “only”  $10^{38}$  luminosity, we estimate that our system will operate at 62% polarization or above, much higher than half-maximum. The parameters that can be varied to achieve that luminosity are: beam current, cell pressure, cell length, and cell temperature.

Here we discuss the effects of cell temperature. We modeled heat transfer assuming laminar gas flow in a tube with the energy deposition balanced by convective heat transfer to the wall and increased enthalpy of the flowing gas, and using the laminar flow formulation to estimate the convective heat transfer. This assumption is conservative. At higher power dissipation rates, convective heat losses will actually be much higher. Large volumetric energy generation generally leads to turbulent buoyancy-driven secondary flows, which greatly increases convective heat losses. Although rigorous analysis of this case requires a computational fluid dynamic simulation, simple analysis provides a lower limit of the target density. Fig. 20 shows variation in target luminosity with system pressure, flow rate, and wall temperature. Increased heating with target density causes luminosity to increase with temperature; however, increasing the flow rate alleviates this effect. We conclude that immersing the target in liquid nitrogen increases the luminosity by a factor two relative to a target cooled with water at 300K (rather than the factor of three one would get from the simple ratio of the temperatures).

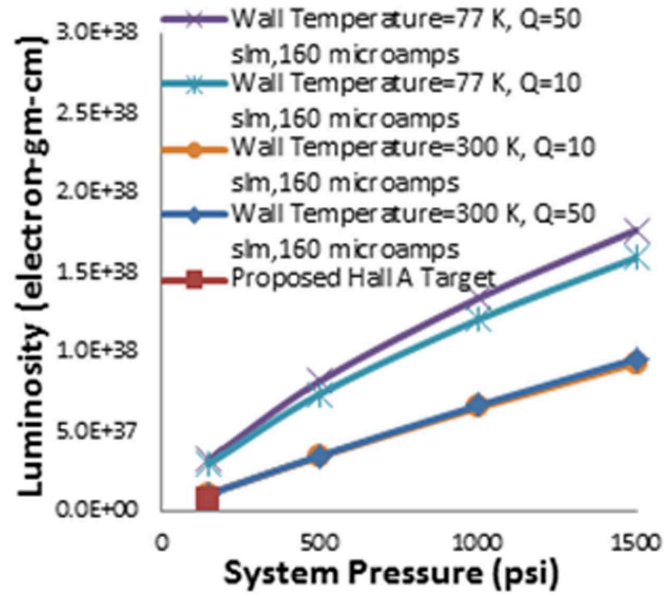


FIG. 20: Luminosity of a high pressure polarized  $^3\text{He}$  target for  $160 \mu\text{A}$  beam current and 40 cm length at 77 K and 300 K at several target pressures and flow rates.